

TESS unveils the phase curve of WASP-33b

Characterization of the planetary atmosphere and the pulsations from the star

C. von Essen^{1,2}, M. Mallonn³, C. C. Borre¹, V. Antoci^{4,1}, K.G. Stassun⁵, S. Khalafinejad⁶, and G. Tautvaišienė²

¹ Stellar Astrophysics Centre, Department of Physics and Astronomy, Aarhus University, Ny Munkegade 120, DK-8000 Aarhus C, Denmark

e-mail: cessen@phys.au.dk

² Astronomical Observatory, Institute of Theoretical Physics and Astronomy, Vilnius University, Sauletekio av. 3, 10257, Vilnius, Lithuania

³ Leibniz-Institut für Astrophysik Potsdam (AIP), An der Sternwarte 16, D-14482 Potsdam, Germany

⁴ DTU Space, National Space Institute, Technical University of Denmark, Elektrovej 328, DK-2800 Kgs. Lyngby, Denmark

⁵ Vanderbilt University, Department of Physics & Astronomy, 6301 Stevenson Center Ln., Nashville, TN 37235, USA

⁶ Landessternwarte, Zentrum für Astronomie der Universität Heidelberg, Königstuhl 12, 69117 Heidelberg, Germany

Received 09.03.2020; accepted 22.04.2020

ABSTRACT

We present the detection and characterization of the full-orbit phase curve and secondary eclipse of the ultra-hot Jupiter WASP-33b at optical wavelengths, along with the pulsation spectrum of the host star. We analyzed data collected by the Transiting Exoplanet Survey Satellite (TESS) during Sector 18. WASP-33b belongs to a very short list of highly irradiated exoplanets that were discovered from the ground and were afterwards visited by TESS. WASP-33b's host star, of δ Scuti type, shows non-radial pulsations in the milli-magnitude regime, with periods comparable to that of the primary transit. These completely deform the photometric light curve, hindering our interpretations. Carrying out a detailed determination of the pulsation spectrum of the host star, we find 29 pulsation frequencies with a signal-to-noise ratio higher than 4. After cleaning the light curve for the stellar pulsations we confidently report a secondary eclipse depth of 305.8 ± 35.5 parts-per-million (ppm), along with an amplitude of the phase curve of 100.4 ± 13.1 ppm and a corresponding westward offset between the region of maximum brightness and the substellar point of 28.7 ± 7.1 degrees, making WASP-33b one of the few planets with such an offset found so far. Our derived Bond albedo, $A_B = 0.369 \pm 0.050$, and heat recirculation efficiency, $\epsilon = 0.189 \pm 0.014$, reconfirm WASP-33b to be similar in behaviour to other hot Jupiters, despite the high irradiation received from its host star. Connecting the amplitude of the phase curve to the primary transit and secondary eclipse depths, we determine the day and night side brightness temperatures of WASP-33b to be 3014 ± 60 K and 1605 ± 45 K, respectively. From the detection of photometric variations due to gravitational interactions, we estimated a planet mass of $M_P = 2.81 \pm 0.53 M_J$. Analyzing the stellar pulsations in the frame of the planetary orbit, we find no signals of star-planet interactions.

Key words. stars: planetary systems – stars: individual: WASP-33 – methods: observational

1. Introduction

Since August, 2018, the Transiting Exoplanet Survey Satellite (TESS, [Ricker et al. 2015](#)) has been scanning the southern and northern ecliptic hemispheres in the search for planets around bright stars. To date (April, 2020), TESS has detected the dim of light during transit of ~ 1800 TESS Objects of Interest (TOIs), out of which ~ 45 have been confirmed as exoplanets¹. Several TESS discoveries include the first Earth-sized planet ([Dragomir et al. 2019](#)), an eccentric massive Jupiter orbiting a sub giant star each 9.5 days ([Rodríguez et al. 2019](#)), and the first multi-planet systems ([Kostov et al. 2019](#); [Günther et al. 2019](#); [Vanderburg et al. 2019](#)).

Besides the detection and characterization of brand-new systems, TESS has also been contributing with the in-depth study of those previously detected from the ground. Some of TESS contributions are the detection of a decrease in the orbital period of WASP-4b ([Bouma et al. 2019](#)), and of particular interest to this work, the characterization of the phase curve and secondary eclipse depth of WASP-18b ([Shporer et al. 2019](#)), WASP-19b

([Wong et al. 2020](#)), WASP-121b ([Bourrier et al. 2019](#); [Daylan et al. 2019](#)), WASP-100b ([Jansen & Kipping 2020](#)), and KELT-9b ([Wong et al. 2019](#)). For WASP-18b, the precision in the photometry allowed [Shporer et al. \(2019\)](#) to unveil sinusoidal modulations across the orbital phase, that were shaped by the atmospheric characteristics of the planet and by the gravitational interactions between the planet and host star. WASP-19b's data revealed a strong atmospheric brightness modulation signal and no significant offset detected between the substellar point and the region of maximum brightness on the day side of the planet, in full agreement with what WASP-121b data showed.

All the mentioned planets with full-orbit phase curves measured by TESS belong to the group of ultra-hot Jupiters. These planets receive such an extreme amount of stellar insolation that they exhibit day side temperatures superior to ~ 2200 K. Similar to hot Jupiters of more moderate temperatures, they are expected to be tidally locked due to their very close proximity to the host star. Another ultra-hot Jupiter observed by TESS is WASP-33b ([Collier Cameron et al. 2010](#)). With a day side temperature close to 3200 K ([Zhang et al. 2018](#)), it belongs to the very top of a temperature ranking of highly irradiated, super hot exoplanets. The planet orbits a δ Scuti star of spectral type A that oscillates

¹ <https://tess.mit.edu/publications/>

with pulsations commensurable to the transit duration and with amplitudes well within the milli-magnitude regime (Smith et al. 2011; Herrero et al. 2011; von Essen et al. 2014). Relevant stellar and planetary parameters can be found in Table 1 and Table 3. So far, the planet has been thoroughly investigated. Among others, observational data have revealed several secondary eclipse depths at different wavelengths (Smith et al. 2011; Deming et al. 2012; de Mooij et al. 2013; Haynes et al. 2015; von Essen et al. 2015), a detailed characterization of the pulsation spectrum of the host star with the goal of determining planetary parameters from pulsation-cleaned light curves (Herrero et al. 2011; von Essen et al. 2014), and the characterization of its atmospheric composition where aluminium oxide was for the first time ever unveiled (von Essen et al. 2019a). In addition to this detection, in high resolution Yan et al. (2019) characterized its transmission spectrum around the individual lines of Ca II H&K, finding it mostly ionized in its upper atmosphere, while Nugroho et al. (2017) found molecular TiO in the day side spectra. Space-based Spitzer observations of WASP-33's phase curves in the near infrared allowed (Zhang et al. 2018) to estimate the planetary brightness temperature, albedo and heat recirculation efficiency, finding WASP-33b to share similarities to hot Jupiters, despite its unusually high irradiation level.

Phase curve observations at TESS optical wavelengths allow for the measurement of the combined reflected and thermally emitted planetary light at a function of longitude. Recent reviews on exoplanet phase curves were provided by Shporer (2017) and Parmentier & Crossfield (2018). For an ultra-hot Jupiter as WASP-33b, we still expect the thermal light component to dominate, being informative on the efficiency of the heat distribution from the insolated day side to the night side. This energy transport is expected to be less efficient for ultra-hot Jupiters compared to hot Jupiters of more moderate temperature due to stronger radiative energy loss and a partial ionization of the atmosphere, preventing strong advective energy transport by a magnetic drag (e.g. Lothringer et al. 2018; Arcangeli et al. 2019). The optical phase curve of WASP-33b, presented in this work, will shed light on the energy recirculation by providing the related observing parameters of day-night temperature contrast and phase curve offset for an extremely irradiated planet. Moreover, a comparison of the optical phase curve results of this work and the NIR phase curve results for the same planet of Zhang et al. (2018) will inform about their wavelength-dependence, and therefore how closely the planet atmosphere is described as a black body.

We show in Sect. 2 a detailed description of the observations used to characterize the secondary eclipse and the phase curve of WASP-33b. In Sect. 3 we present our analysis over the third light contamination (Sect. 3.1), our update on the transit parameters (Sect. 3.5) and our strategy to clean the light curves from transits to use them to determine the pulsation spectrum of the host star (Sect. 3.3). We introduce our models interpreting WASP-33b's secondary eclipse and phase curve in Sect. 4.3. In Section 5 we provide a detailed discussion about the impact of the pulsations over the derived atmospheric parameters (Sect. 4.7), we derive relevant physical parameters in Sections 5.1 and 5.2, we place WASP-33b and our results in context in Section 5.3, and we update the stellar and planetary parameters in Section 3.6. We finish this work with some conclusive remarks under Sect. 6.

2. Observations

WASP-33 (TIC identifier 129979528) was observed by TESS in sector 18, more specifically between November 3rd and 26th,

2019, during cycle 2 and using camera 1. The data have a cadence of 120 seconds and were analyzed and detrended by the Science Processing Operations Center (SPOC) pipeline, based on the NASA Kepler mission pipeline (Jenkins et al. 2016; Jenkins 2017). Time stamps are given in Barycentric Julian Dates (BJD_{TDB}), and are in consequence not converted to other time reference frame.

The light curve of WASP-33 can be seen in Fig. 1. The total time on target is of about 23 days, during which 16 primary transits were observed. The first ~800 data points were not considered in our analysis, as they show some noise structure which we believe is extrinsic to the star. An initial analysis was done over both Simple Aperture Photometry (SAP) and Presearch Data Conditioning (PDC) light curves (Smith et al. 2012; Stumpe et al. 2014), after which we decided to work on the SAP data using our own normalization strategy (see Section 3.4 for a motivation of our choice). To prepare the data for analysis, we first removed all flag points, both in time or in flux. Then, we binned the points each 8 hours to minimize the impact of the normalization on the stellar pulsations, after which we interpolated a spline function. We used this to normalize the data and to remove outliers that were 5 times the standard deviation away. The removed points are of the order of 100, and the total data points analyzed in this work are 14000.

3. Analysis and model considerations

3.1. Third light contamination

When analyzing photometric time series including exoplanetary primary transits, special care has to be taken. In certain cases, light of another star than the planetary host is included inside the chosen photometric aperture, diluting the depth of the primary transits (see e.g., Piskorz et al. 2015; Mugrauer 2019; Belokurov et al. 2020, for large systematic search of companions nearby exoplanets). TESS cameras have a pixel size of 21×21 arcseconds. Under these circumstances, when a light curve is constructed by co-adding the light of several pixels (see Fig. 2, top), it is very likely that the aperture will include light from other stars than that of the host (Figure 2, bottom).

WASP-33's first identified companion, WASP-33B, lies at an angular separation of ~2 arcseconds and is, in consequence, included inside the TESS aperture. The sub-stellar object was first reported by Moya et al. (2011) and then confirmed by Adams et al. (2013); Wöllert & Brandner (2015); Ngo et al. (2016). Using years of follow-up observations, Ngo et al. (2016) carried out a combined analysis and pinpointed WASP-33 as a binary system candidate. Nowadays, WASP-33 has been identified as a hierarchical triple star system (Mugrauer 2019) with a second companion, WASP-33C, ~49 arcseconds away from the planet-host star. Owing to its orientation (South-East from WASP-33), WASP-33C is in principle not included inside TESS aperture. However, due to the large point spread function of TESS, some light of WASP-33C might be included. Unfortunately, there is no way to quantify this than by comparing the derived transit depth to literature values and/or those expected from atmospheric models. A third star, located 23 arcseconds North-West from WASP-33 (Gaia DR2 328636024020571008, Gaia Collaboration et al. 2018, $G = 14.6173 \pm 0.0005$) is included in the aperture. Even though the SPOC pipeline provides an estimation of the stellar crowding contamination, we thought prudent to contrast this with that determined from our own analysis. In consequence, prior to the transit fitting we computed the third light contribution of WASP-33's companions

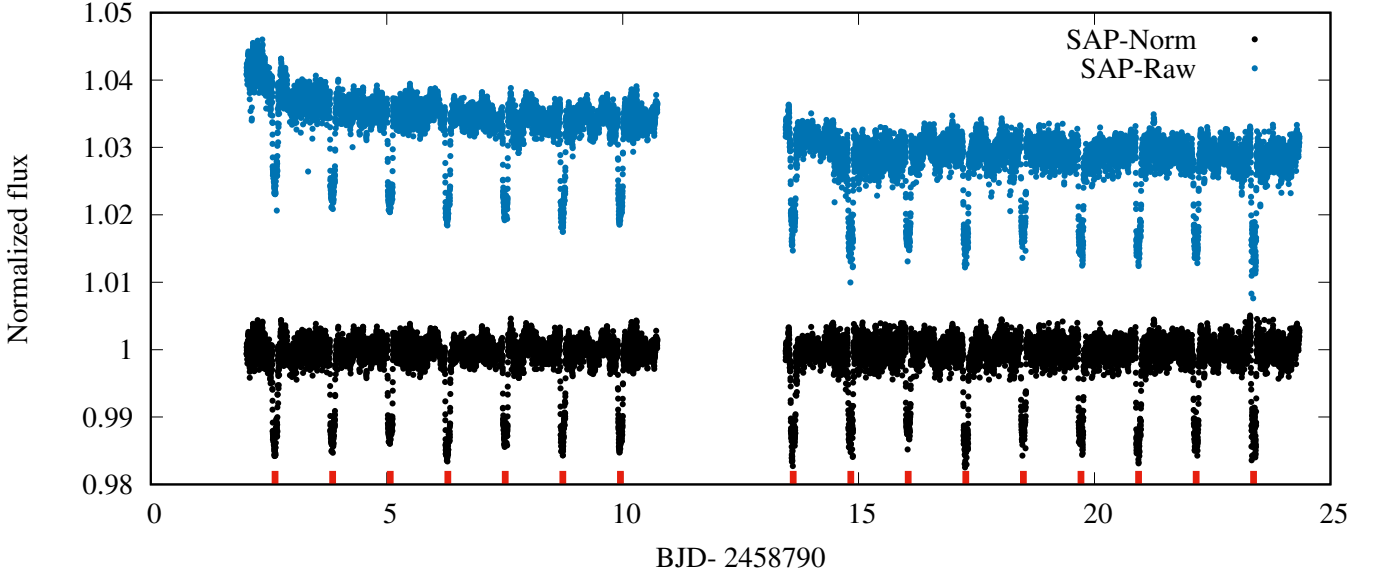


Fig. 1: Simple Aperture Photometry (SAP) normalized flux of WASP-33 observed by TESS in black circles, along with SAP raw data in blue. The pulsations of the star deform the continuum level. The sixteen transits are indicated in the bottom of the figure with red lines. The gap in the middle is caused by data downlink dead time.

within TESS transmission response, namely that of WASP-33B and Gaia DR2 328636024020571008, and compared this to the value reported in the header of WASP-33’s fits file, specifically under the CROWDSAP keyword.

Due to the nature of the system it is safe to assume WASP-33 and WASP-33B to be at the same distance. In consequence, we reproduced their emission with PHOENIX synthetic spectra (Gttingen 2018) without the need of scaling the fluxes further to account for distances. Specifically, we used PHOENIX spectra with basic stellar parameters (T_{eff} , $[\text{Fe}/\text{H}]$, $\log(g)$) matching those of WASP-33 (Collier Cameron et al. 2010) and of the close-in companion (Ngo et al. 2016) as summarised in Table 1.

After convolving PHOENIX intensities with TESS transmission response, we integrated the remaining fluxes and computed their ratio. In this fashion, we obtain a third light contribution of WASP-33B to be $F_{\text{W33B}}/F_{\text{W33}} = 0.018$.

The case of Gaia DR2 328636024020571008 is slightly different as it is not bound to WASP-33 by gravity, not allowing us to assume equal distances. Gaia Collaboration et al. (2018) estimated its temperature to be ~ 5075 K, so we represented its emission using PHOENIX synthetic spectra for a main sequence star of $T_{\text{eff}} = 5000$ K. To compensate for the difference in distance, we computed Gaia’s magnitude difference between WASP-33 ($G = 8.0700 \pm 0.0004$) and this star, and we scaled PHOENIX flux ratios of WASP-33 and Gaia DR2 328636024020571008 integrated within Gaia’s transmission response to meet the magnitude difference. Then, we used this factor to scale down the spectra inside TESS transmission response. Like this, the third light contribution of Gaia DR2 328636024020571008 was found to be $F_{\text{Gaia}}/F_{\text{W33}} = 0.006$. The total third light contribution used in our model is the addition of these two, and equal to $\Delta F = 0.024$. In comparison, the value reported under CROWDSAP is 0.9789 , equivalently $1 - 0.9789 = 0.0211$, to be compared to our ΔF . As both values differ only $\sim 10\%$, we find the two values compatible and from this point and onward, we will use our derived value to correct for third light.

3.2. Limb-darkening coefficients

In this work we adopted a quadratic limb-darkening law:

$$\frac{I(\mu)}{I(1)} = 1 - u_1(1 - \mu) - u_2(1 - \mu)^2, \quad (1)$$

with corresponding linear (u_1) and quadratic (u_2) limb-darkening coefficients (LDCs). In the equation, $I(1)$ is the specific intensity at the centre of the stellar disk and $\mu = \cos(\gamma)$, where γ is the angle between the line of sight and the emergent intensity. To compute our custom limb-darkening coefficients that meet TESS transmission response we used angle-dependent, specific intensity spectra from PHOENIX (Gttingen 2018) with main stellar parameters corresponding to the effective temperature, $T_{\text{eff}} = 7400$ K, surface gravity, $\log(g) = 4.5$, and metallicity, $[\text{Fe}/\text{H}] = 0.00$, matching the values of WASP-33 reported in Table 1 within uncertainties. As similarly done by von Essen et al. (2017) and Claret & Bloemen (2011), we neglect the data points between $\mu = 0$ and $\mu = 0.07$, as the intensity drop given by PHOENIX models is too steep and potentially unrealistic. After integrating the PHOENIX angle-dependent spectra convolved by TESS response, we fitted the derived intensities normalized by its maximum values with Equation 1 using a MCMC approach. The derived limb-darkening coefficients for WASP-33 are $u_1 = 0.246(6)$ and $u_2 = 0.252(6)$. Errors for the coefficients are derived from the posterior distributions of the MCMC chains, after visually inspecting them for convergency. In order to assess the quality of our procedure, we fitted the LDCs to TESS primary transit light curves. From their posterior distributions we obtained consistent results with their PHOENIX counterparts. Our derived LDCs are well compared to those from Claret (2017) ($u_1 = 0.2446$ and $u_2 = 0.2449$). A word of caution has to be given here. Even though the precision of our fit lies in the fourth decimal, LDCs drag unspoken errors from the lack of precision of, for instance, stellar intensities. In consequence, we disbelieve that the precision from the fit reflects the real precision at which we know any limb-darkening coefficient. Based

Table 1: Effective temperature, metallicity and surface gravity for WASP-33 and the stars included in TESS aperture.

Parameter	WASP-33 (Collier Cameron et al. 2010)	WASP-33B (Ngo et al. 2016)	Gaia DR2 328636024020571008 Gaia Collaboration et al. (2018)
T_{eff} (K)	7430 ± 100	3050 ± 250	5074.75
[Fe/H]	0.1 ± 0.2	0 (adopted)	0 (adopted)
$\log(g)$	4.3 ± 0.2	5 (Angelov 1996)	4.5 (Angelov 1996)

Target ID: 129979528, Cadence: 405505

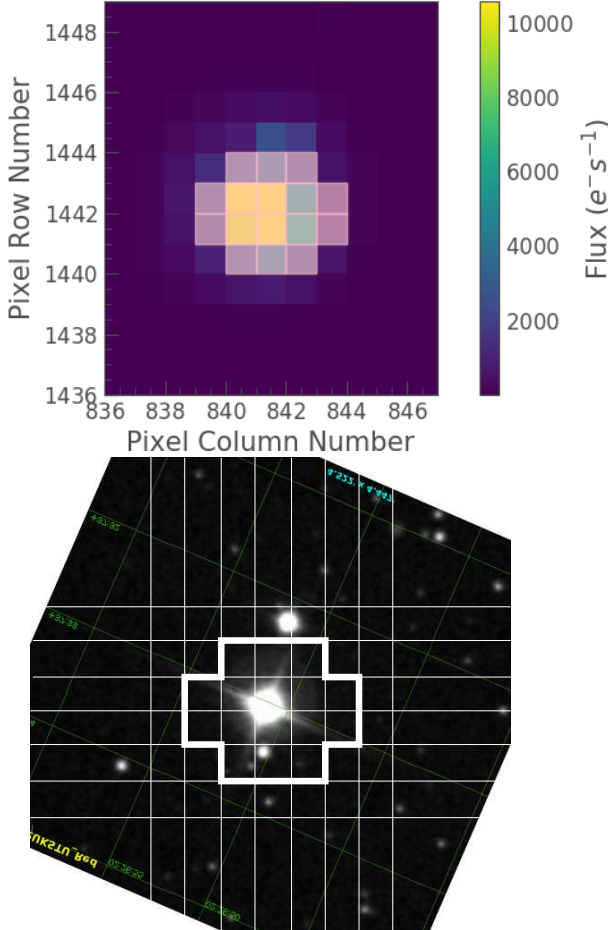


Fig. 2: *Top*: Target Pixel File (TPF) of WASP-33 showing the chosen aperture mask. No stars can be visually resolved. *Bottom*: $\sim 4 \times 4$ arcmin field of view centered around WASP-33. The mask and the pixels are schematized with white thick and thin lines, respectively. WASP-33C, the bright star south from WASP-33, is not included in the aperture. The field of view has been rotated to be aligned with the ecliptic system, and is oriented to coincide with the images given in TESS’s summary report.

on this assumption, in order to reduce computational cost in this work we consider u_1 and u_2 as fixed.

3.3. Pulsation spectrum of the host star

The pulsation frequencies of the host star were determined using Period04 (Lenz & Breger 2005), after the primary transits were fitted and removed. The complete procedure was carried out over both SAP and PDC light curves, obtaining consistent results. The software uses a Fast Fourier Transform to calculate the power spectrum, and simultaneous least square fitting to derive

the pulsation frequencies, their amplitudes and phases. These were extracted one by one, starting with the one having the largest amplitude. We considered a peak to be statistically significant only if it was resolved, and if its corresponding signal-to-noise ratio (SNR) was larger or equal to 4 (see e.g., Breger et al. 1993; von Essen et al. 2014). The SNR was calculated using the default setting, i.e., a window of 2 cycles/day (cd^{-1}) around each peak. We estimated the uncertainties using Period04 MCMC’s tool. These are produced as described in Breger et al. (1999), and are given at a $1-\sigma$ level and derived from 1000 MCMC iterations. The amplitude uncertainties depend only on the residuals and the number of data points in the time series, which explains why all the values are the same.

The power spectrum of WASP-33 is shown in Fig. 3, and the 29 extracted pulsation frequencies, with their associated amplitudes and phases are given in Table 2. For completeness, we provide a comparison to the peaks found by von Essen et al. (2014).

Two frequencies identified by von Essen et al. (2014) were not reproduced in this analysis, namely 8.308 cd^{-1} (Puls₇) and 10.825 cd^{-1} (Puls₈). Both are located in a frequency range with slightly higher noise level in the TESS data, which is likely to be due to additional unresolved pulsation modes originating from the star. As a consequence, it is not clear whether these peaks have now a lower amplitude than before and are therefore buried in the noise, or whether the peaks identified before may have been the result of aliases. It shall be noted that δ Sct-type pulsations are known to show (sometimes strong) amplitude variability over time (see e.g., Bowman & Kurtz 2018). In addition, the TESS bandpass is redder than the filters used in von Essen et al. (2014), which implies that the pulsation amplitudes are expected to be lower as well, also depending on the exact geometry of the mode. WASP-33 displays p-mode oscillations at high frequencies, which is characteristic for δ Scuti stars (see, e.g., Aerts et al. 2010; Antoci et al. 2019). Owing to the 23 days of continuous monitoring provided by TESS data, we also detected statistically significant peaks at lower frequencies (namely F2 and F5 in Table 2). If these are independent pulsation modes, they would correspond to g-mode pulsations typical for γ Doradus stars (see, e.g., Aerts et al. 2010; Li et al. 2020). Showing both g and p-mode pulsations, WASP-33 would then fall into the γ Doradus/ δ Scuti hybrid classification (Grigahcène et al. 2010; Balona & Dziembowski 2011; Uytterhoeven et al. 2011). However, with only two peaks detected at low frequencies, we prefer to wait for more data before classifying WASP-33 as such. In von Essen et al. (2014), signals with frequencies lower than $\sim 7 \text{ cd}^{-1}$ were not detectable. Besides the obvious gaps produced by the day-night cycle, the data were normalized on a nightly basis, removing in consequence the long trends. Also, due to poor weather conditions the observations could not be produced along consecutive nights, and had on average a ~ 5 hour duration. A longer time series than the one provided by TESS could resolve the pulsations at lower frequencies, and thereby determine if the star is purely a δ Scuti or a hybrid star.

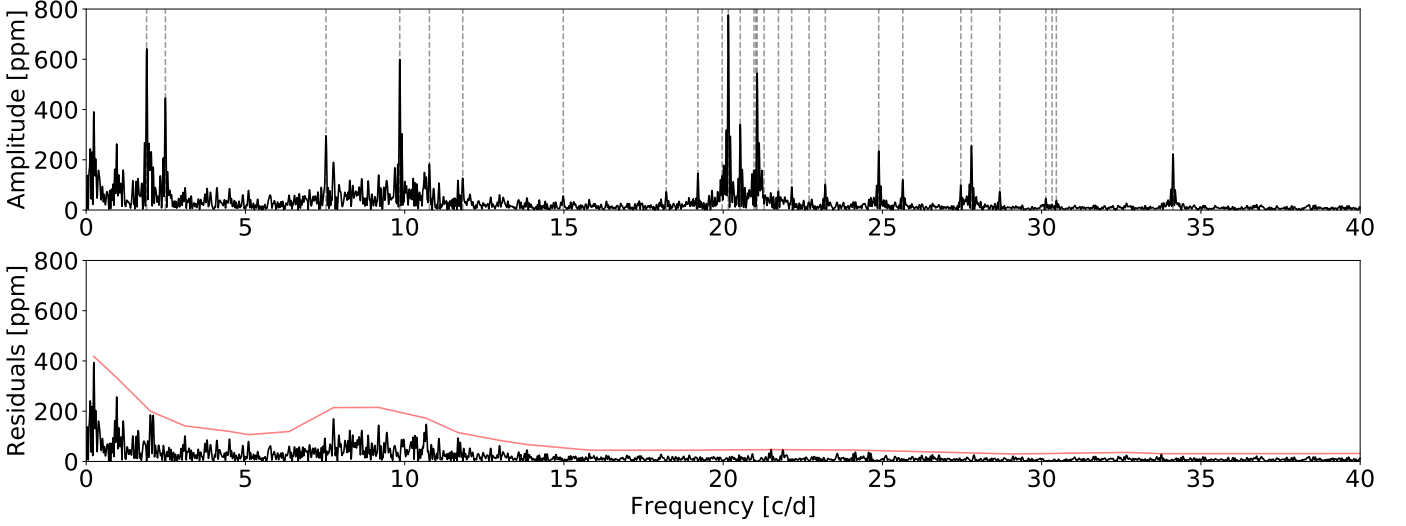


Fig. 3: Top panel: Power spectrum of WASP-33. Pulsations are marked with dashed gray lines. Bottom panel: Residuals after frequency extraction. The red line makes the SNR limit of 4.

Table 2: Pulsation frequencies of WASP-33 derived from TESS photometry. From left to right we present the frequency number, F#, arranged in decreasing amplitude, the frequency, in cd^{-1} , the amplitude, in ppm, the phase, in units of 2π , and the frequency, in cP^{-1} . In all cases errors are given at $1-\sigma$ level. The last column shows the frequencies obtained in [von Essen et al. \(2014\)](#), coinciding to the ones found here.

F#	Frequency (cd^{-1})	Amplitude (ppm)	Phase (2π)	Frequency (cP^{-1})	Frequency (von Essen et al. 2014 , cd^{-1})
F1	20.16263 ± 0.00032	772 ± 10	0.4904 ± 0.0020	24.5957 ± 0.0004	20.16214 ± 0.00063 (Puls ₁)
F2	1.89739 ± 0.00038	648 ± 10	0.0084 ± 0.0024	2.3145 ± 0.0004	-
F3	9.84567 ± 0.00041	604 ± 10	0.4927 ± 0.0026	12.0104 ± 0.0005	9.84361 ± 0.00066 (Puls ₃)
F4	21.06527 ± 0.00043	564 ± 10	0.3151 ± 0.0028	25.6968 ± 0.0005	21.06057 ± 0.00058 (Puls ₂)
F5	2.48691 ± 0.00052	468 ± 10	0.6578 ± 0.0034	3.0337 ± 0.0006	-
F6	20.53605 ± 0.00073	334 ± 10	0.2175 ± 0.0047	25.0512 ± 0.0008	20.53534 ± 0.00057 (Puls ₅)
F7	7.52946 ± 0.00083	296 ± 10	0.5895 ± 0.0053	9.1849 ± 0.0010	-
F8	27.79525 ± 0.00096	256 ± 10	0.9856 ± 0.0062	33.9065 ± 0.0011	-
F9	24.8835 ± 0.0010	243 ± 10	0.9808 ± 0.0065	30.3545 ± 0.0012	24.88351 ± 0.00056 (Puls ₄)
F10	34.1254 ± 0.0011	220 ± 10	0.9392 ± 0.0072	41.6284 ± 0.0013	34.12521 ± 0.00054 (Puls ₆)
F11	20.9668 ± 0.0012	198 ± 10	0.9824 ± 0.0080	25.5767 ± 0.0014	-
F12	10.7773 ± 0.0013	184 ± 10	0.0815 ± 0.0086	13.1468 ± 0.0015	-
F13	11.8238 ± 0.0019	130 ± 10	0.385 ± 0.012	14.4234 ± 0.0023	-
F14	25.6394 ± 0.0021	118 ± 10	0.854 ± 0.013	31.2766 ± 0.0025	-
F15	19.2058 ± 0.0021	116 ± 10	0.986 ± 0.014	23.4285 ± 0.0025	-
F16	23.2070 ± 0.0023	107 ± 10	0.075 ± 0.015	28.3094 ± 0.0028	-
F17	19.9681 ± 0.0024	104 ± 10	0.331 ± 0.015	24.3584 ± 0.0029	-
F18	27.4616 ± 0.0028	88 ± 10	0.165 ± 0.018	33.4995 ± 0.0034	-
F19	21.7361 ± 0.0031	80 ± 10	0.267 ± 0.020	26.5151 ± 0.0037	-
F20	22.1513 ± 0.0032	76 ± 10	0.686 ± 0.021	27.0216 ± 0.0039	-
F21	21.0256 ± 0.0034	72 ± 10	0.203 ± 0.022	25.6484 ± 0.0041	-
F22	28.68628 ± 0.0035	69 ± 10	0.127 ± 0.023	34.9934 ± 0.0042	-
F23	18.2134 ± 0.0036	69 ± 10	0.611 ± 0.023	22.2179 ± 0.0044	-
F24	21.2856 ± 0.0037	67 ± 10	0.064 ± 0.024	25.9656 ± 0.0045	-
F25	14.9793 ± 0.0045	55 ± 10	0.754 ± 0.029	18.2727 ± 0.0054	-
F26	30.1311 ± 0.0051	48 ± 10	0.415 ± 0.033	36.7559 ± 0.0062	-
F27	22.6975 ± 0.0052	47 ± 10	0.123 ± 0.034	27.6879 ± 0.0063	-
F28	30.4605 ± 0.0064	39 ± 10	0.585 ± 0.041	37.1577 ± 0.0078	-
F29	30.3283 ± 0.0088	28 ± 10	0.779 ± 0.056	36.9965 ± 0.0107	-

3.4. Noise treatment

Previous studies similar to this one, but based on other targets (see e.g., [Bourrier et al. 2019](#); [Wong et al. 2020](#)), demonstrated how PDF data showed additional time-correlated residual features in the photometry that were not present in the SAP light curves. Usually, the authors carry out their own detrending strat-

egy over SAP data and use these results as base for their analysis. In our case, we have strong intrinsic variability of the star manifested as stellar pulsations, which amplitudes are larger than the time-correlated features mentioned before. As the pulsations hinder the possibility of properly analyzing the residual noise in our light curves, our approach in this work is slightly dif-

ferent. First, it is worth to repeat that the criteria to consider a pulsation as detected is based over a very tight constrain of amplitude signal-to-noise ratio, $\text{ASNR} > 4$, which is in turn determined around a box of 2 cd^{-1} , as detailed before. This constrain is significantly tighter than, for example, the use of the false alarm probability over a periodogram to claim the detection of a pulsation frequency. Thus, the detected pulsations are robust, despite the residual features of the PDF. Additionally, even though we have characterized the pulsation spectrum of the host star as never done before, there are residual pulsations in TESS photometry. To take into consideration the impact of the residual features in the PDF data that we can not clearly characterize, and the residual pulsation features left after accounting for our derived 29 pulsation frequencies in both SAP and PDF light curves, we computed in both cases the β factor, as specified by [Carter & Winn \(2009\)](#), and used the minimization of the β factor as tool to decide which data set to use. To quantify to what extent TESS photometry is affected by systematic noise, we computed residuals for both PDC/SAP data subtracting the primary transit light curves and the 29 pulsation frequencies. We then divided the residuals into M bins of equal duration, with N equal to the number of data points per bin. If the residuals are not affected by red noise, they should follow the expectation of independent random numbers,

$$\sigma_N = \sigma_1 N^{-1/2} [M/(M-1)]^{1/2}, \quad (2)$$

where σ_1^2 is the sample variance of the unbinned data and σ_N^2 is the sample variance (or RMS) of the binned data, with the following expression:

$$\sigma_N = \sqrt{\frac{1}{M} \sum_{i=1}^M (\langle \hat{\mu}_i \rangle - \bar{\mu})^2}. \quad (3)$$

In the equation, $\hat{\mu}_i$ is the mean value of the residuals per bin, and $\langle \hat{\mu}_i \rangle$ is the mean value of the means. In the presence of correlated noise, each σ_N differs by a factor of β_N from their expectation. The β factor, used to enlarge the individual photometric errors, is nothing more than an average of β_N 's computed considering different time scales, Δt , that are judged to be most important. In our case, the nature of the noise –and thus the relevant timescales– differ drastically. Thus, to compute β_N we considered Δt between 2 hours (systematics due to residual pulsations) and 4 days (systematics due to PDM detrending), divided in steps of 1 hour, corresponding to a total of 94 Δt 's. Figure 4 shows our resulting β_N 's as a function of the frequency ($1/\Delta t$). Note that, in both cases, the highest β_N values are in the lower end of the frequency range, where TESS total time coverage does not allow us to resolve the pulsation frequencies from the high noise. As the figure shows, there is a drastic increase of β_N from SAP to PDC photometry, almost increasing a factor of three. The corresponding β factors are computed from the average of the β_N 's, with values $\beta_{\text{SAP}} = 3.545$, and $\beta_{\text{PDC}} = 8.609$. In consequence, this work is based on SAP data, where the individual error bars are increased by a factor of 3.545.

3.5. Primary transit parameters from TESS light curves

In [von Essen et al. \(2014\)](#) we derived the transit parameters accounting and not accounting for the intrinsic variability of the host star. After comparing the derived parameters, we found no significant differences in both sets. The analysis of TESS data revealed no different results, which were derived in the following way. First, we analyzed TESS data with all the pulsation

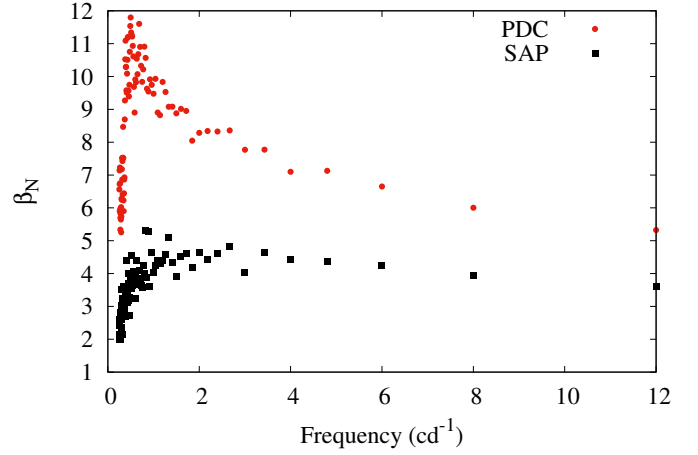


Fig. 4: Correlated noise in TESS photometric products. β_N 's as a function of frequency ($1/\Delta t$) for PDC (red circles) and SAP (black squares) data sets.

frequencies still included. We considered the data points around ± 0.1 days centered in each mid-transit time, to have enough off-transit data to normalize each transit. For the normalization we used a second order time-dependent polynomial, that was fitted simultaneously to the transit model ([Mandel & Agol 2002](#)). The degree of the polynomial was chosen from a prior analysis of the data, trying as detrending functions a first, second, and third degree time-dependent polynomial. After carrying out a simple least-squared fit between the primary transits and the detrending times the transit model, we computed the Bayesian Information Criterion (BIC) from the residuals, and analyzed which polynomial systematically minimized the BIC. The fitting parameters are the semi-major axis, a/R_S , the inclination in degrees, i , the orbital period, P , the planet-to-star radius ratio, R_P/R_S , and the mid-transit time of reference, T_0 . As specified before, we used a quadratic limb-darkening law. In this work, we consider the eccentricity fixed and equal to zero ([Smith et al. 2011](#)). Our joined model includes $3 \times \text{TN} + 5$ parameters, where $\text{TN} = 16$ corresponds to the total number of transits, 3 to the number of coefficients for the detrending polynomial, and 5 accounts for the primary transit parameters previously mentioned. The transit light curves, along with the derived best-fit transit model, are shown in Figures A.1 and A.2 in black points and red continuous line, respectively. Subsequently, we analyzed TESS data after removing all the pulsation frequencies listed in Table 2, specifically dividing away from the fluxes the summation of the 29 pulsation frequencies using the following equation:

$$\text{PM}(t) = \sum_{i=1}^{29} A_i \times \sin[2\pi(t\nu_i + \phi_i)], \quad (4)$$

where A_i , ν_i and ϕ_i are the amplitudes, frequencies and phases listed in Table 2, respectively. The number of fitting parameters and the degree of the detrending function stayed unchanged. All the primary transit light curves cleaned from the 29 pulsation frequencies, along with the best-fit transit model, are also shown in Figures A.1 and A.2, vertically shifted down to allow for visual comparison. To derive the best-fit values for the model parameters and their corresponding uncertainties we used a Markov-chain Monte Carlo (MCMC) approach, all implemented in rou-

tines of PyAstronomy² (Patil et al. 2010; Jones et al. 2001). We iterated 1 000 000 times, with a conservative burn-in of the first 20% samples. For all the parameters we considered uniform priors around $\pm 50\%$ their corresponding starting values. These were taken from von Essen et al. (2014) for the primary transit model, specified in the last column of Table 3. Starting values for each second order time-dependent polynomial were derived from a simple least-square minimization. We computed the median and standard deviation from the posterior distributions, and used these as our best-fit values and uncertainties, given at $1-\sigma$ level. We checked the convergence of the chains by visually inspecting each one of them, and by dividing the chains in three sub-chains. In each case, we computed the usual statistics and we considered that a chain converged if the derived parameters were consistent within their uncertainties.

The ephemerides following from 23 days of TESS data, derived from our transit fitting accounting for the stellar pulsations, are the following:

$$\begin{aligned} T_0 &= 2458792.63403 \pm 0.00009 \text{ BJD}_{\text{TDB}} \\ \text{Per} &= 1.2198681 \pm 4.2 \times 10^{-6} \text{ days} \end{aligned}$$

Our derived period agrees within $1-\sigma$ to the one reported by Maciejewski et al. (2018). Both semi-major axis and inclination agree at the same level with the corresponding values reported in von Essen et al. (2014). The only exception is the planet-to-star radii ratio. Even though this value does not agree with von Essen et al. (2014)'s, it perfectly agrees with the aluminium oxide model extrapolated to TESS wavelengths (see e.g., von Essen et al. 2019a; Welbanks et al. 2019). This value also evidences the accuracy on our treatment for third light contribution. The phase-folded primary transit light curves are shown in Figure 5, not accounting (left) and accounting (right) for the intrinsic variability of the host star. Note the asymmetry in the transit shape that the improper treatment of the pulsation frequencies can cause. For further analysis, we will solely consider the transit parameters listed on the third column of Table 3.

The posterior distributions and the corresponding correlations between parameters can be seen in Fig. 6. Besides the well known correlation between a/R_s and i , and to a lesser extend between P and T_0 , the remaining parameters are uncorrelated, with Pearson's correlation values ranging between -0.05 and 0.04.

3.6. Updated stellar and planetary parameters

We have redetermined the stellar and planetary radii and masses, making advantage of the newly available parallax from *Gaia* DR2 together with the available photometry from all-sky broadband catalogs. We used the semi-empirical approach of measuring the stellar spectral energy distribution (SED) described by Stassun et al. (2017) and Stassun & Torres (2016).

We pulled the $B_T V_T$ magnitudes from *Tycho-2*, the *uvby* magnitudes from Strömgren *uvby* magnitudes from Paunzen (2015), the *JHK_S* magnitudes from 2MASS, the W1–W4 magnitudes from *WISE*, and the *GG_{BP}GRP* magnitudes from *Gaia*. Together, the available photometry spans the full stellar SED over the wavelength range $0.35\text{--}22 \mu\text{m}$ (see Fig. 7).

We performed a fit using Kurucz stellar atmosphere models, with the priors on effective temperature (T_{eff}), surface gravity ($\log g$), and metallicity ($[\text{Fe}/\text{H}]$) from the values reported in Table 1. The remaining free parameter is the extinction, A_V , which we limited to the maximum for the line of sight from the

dust maps of Schlegel et al. (1998). The resulting fit (Fig. 7) is very good, with a reduced χ^2 of 2.7, and best-fit $A_V = 0.04 \pm 0.04$. Integrating the (unreddened) model SED gives the bolometric flux at Earth of $F_{\text{bol}} = 1.455 \pm 0.051 \times 10^{-8} \text{ erg s}^{-1} \text{ cm}^{-2}$. Taking the F_{bol} and T_{eff} together with the *Gaia* DR2 parallax, adjusted by $+0.08$ mas to account for the systematic offset reported by Stassun & Torres (2018), gives the stellar radius as $R_\star = 1.561 \pm 0.052 R_\odot$. Estimating the stellar mass from the empirical relations of Torres et al. (2010) gives $M_\star = 1.59 \pm 0.10 M_\odot$, which is consistent with that inferred from the spectroscopic $\log g$ together with the radius ($1.77 \pm 0.82 M_\odot$). Finally, the estimated mass together with the radius gives the mean stellar density $\rho_\star = 0.59 \pm 0.07 \text{ g cm}^{-3}$.

With the updated value for the stellar radius and the planet-to-star radii ratio derived fitting TESS photometry, we report here the planetary radius in the TESS passband, $R_p = 1.627 \pm 0.054 R_J$.

3.7. Star-planet interaction

Compared to von Essen et al. (2014), the quality of TESS data allowed us to carry out a more thorough analysis of the pulsation spectrum of the host star. As we now count almost 4 times more pulsation frequencies than before, we investigated again if any of the observed pulsations were induced by planetary tides over the star.

To begin with, we do not find a non-radial mode around $\sim 4 \text{ cd}^{-1}$ as previously reported by Collier Cameron et al. (2010). In addition to this, tidally excited modes can be manifested by the commensurability between the orbital period of the planet and the pulsation frequencies (see, e.g. Hambleton et al. 2013). Similarly to von Essen et al. (2014), we used our best-fit orbital period to express the pulsation frequencies as cycles per orbital period (cP^{-1}). These are given in the fifth column of Table 2. We found the closest commensurability to be 36.99669 cP^{-1} , corresponding to the frequency $30.3283 \pm 0.0088 \text{ cd}^{-1}$. The difference to its closest integer number is equal to 0.00331. To assess if this difference is significant enough to pinpoint this pulsation as being triggered by planetary tides, we carried out the same exercise as the one described in von Essen et al. (2014). Briefly, we randomly generate 29 frequencies between the lowest and the highest detected ones, that are in turn derived from a uniform distribution. Then, we convert these frequencies given in cd^{-1} to cP^{-1} , and among these we select the one closest to an integer number, computing their difference. We call this difference the "best match". After 1×10^6 iterations, we compute the cumulative probability distribution for the minimum distance from an integer frequency ratio, d_{min} , as:

$$F(d_{\text{min}}) = 1 - e^{-d_{\text{min}}/\nu} \quad (5)$$

where ν is obtained from fitting our Monte-Carlo results with an exponential decay (see Figure 8). The derived value is $\nu = 0.0078 \pm 0.0007$. From this, we can determine that the probability of finding at least one of the ratios closer than 0.00331 c/per to an integer ratio, among 29 randomly produced pulsation frequencies, is 35%. This value is too high to confidentially claim this particular pulsation to be induced by the planet. In consequence, we find very unlikely that the system is showing evidences of star-planet interactions.

² www.hs.uni-hamburg.de/DE/Ins/Per/Czesla/PyA/PyA/index.html

Table 3: Best-fit transit parameters obtained from TESS photometry (this work), compared to those determined by von Essen et al. (2014), accounting for pulsations.

Parameter	This work (not accounting for pulsations)	This work (accounting for pulsations)	von Essen et al. (2014) (accounting for pulsations)
a/R_S	3.605 ± 0.009	3.614 ± 0.009	3.68 ± 0.03
i ($^\circ$)	88.05 ± 0.28	88.01 ± 0.28	87.90 ± 0.93
R_P/R_S	0.10716 ± 0.00023	0.10714 ± 0.00024	0.1046 ± 0.0006
P (days)	$1.2198696 \pm 4.2 \times 10^{-6}$	$1.2198681 \pm 4.2 \times 10^{-6}$	$1.2198675 \pm 1.5 \times 10^{-6}$
T_0 (BJD _{TDB})	$2458792.63376 \pm 0.00009$	$2458792.63403 \pm 0.00009$	2455507.5222 ± 0.0003

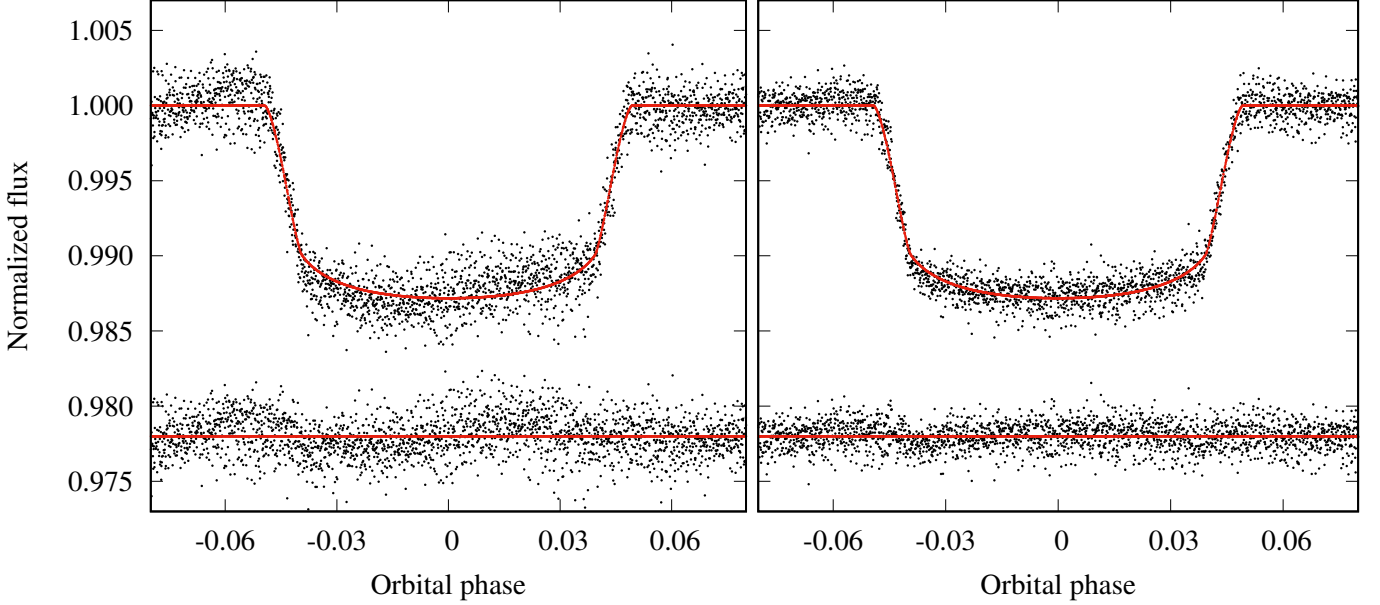


Fig. 5: Primary transit light curves not accounting for (left) and accounting for (right) stellar pulsations. Black points correspond to TESS data, and red continuous line to the derived best-fit transit model. Corresponding residuals are shown below each transit.

4. Joint model

4.1. Fitting strategy

Our model is the addition of five components that are explained in detail next, fitted to the unbinned TESS photometry in simultaneous, once the most prominent pulsations were removed (see Section 4.7). Equivalently to the primary transit fitting approach, to derive the best-fit values of our model we made use of MCMC. In this case, we iterated 10 000 times, with a burn-in of the first 2000 samples, after visually inspecting the chains for convergence. The best-fit values for the parameters, along with their corresponding $1-\sigma$ uncertainties, are derived from the median and standard deviation of the posterior distributions, regardless the use of uniform or Gaussian priors.

To reduce the number of fitting parameters, if a given parameter is present in different model components, these are treated as equal by our MCMC algorithm. For each model component we detail the model parameters, differentiating those fitted on their own and those treated as equal by our MCMC algorithm. In all cases, the variable t corresponds to the time provided by TESS. To be certain that our results are not affected by our choice of priors, and to investigate if the planetary mass has any impact in our modelling, we carried out four different fits in parallel. Model 1 (M1) has uniform priors on all the parameters and considers the planetary mass as fixed. Model 2 (M2) has Gaussian priors on all the parameters and considers the planetary mass as fixed. Model 3 and Model 4 (M3, M4) are similar to M1 and M2,

with the difference that the planetary mass is considered as a fitting parameter. When using uniform priors we considered physically reasonable ranges always fulfilling a conservative $\pm 50\%$ of each parameter, and when using Gaussian priors we either considered the best-fit values and uncertainties derived in this work and specified on the third column of Table 3 as starting values and errors, or we used those from the literature when not available from this work, as for instance with the planetary mass. In both cases, to be conservative the uncertainties were enlarged a factor of 3 when using them as part of the Gaussian priors. At the end of this section we provide the four sets of results, and report as final values those corresponding to the smallest reduced chi-squared. Particularly, for the case of the ellipsoidal variation (Section 4.5) and the Doppler beaming (Section 4.6) we follow the prescription provided and fully described by Beatty et al. (2019), so we do not repeat them in this work.

4.2. Primary transit model

We modelled WASP-33b's primary transit model (TM(t)) as specified before, using Mandel & Agol (2002) model and our custom linear and quadratic limb darkening coefficients. The fitting parameters, namely the semi-major axis, a/R_S , the inclination in degrees, i , the orbital period, P , the planet-to-star radius ratio, R_P/R_S , and the mid-transit time of reference, T_0 , are all parameters that impact the different model components and, in consequence, are always treated as equal. It is worth to men-

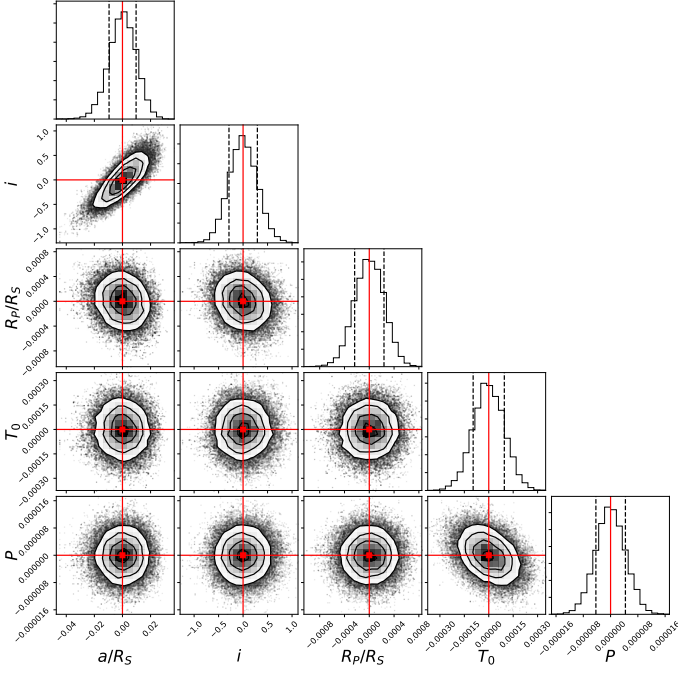


Fig. 6: Posterior distributions for the primary transit parameters fitted in this work. Gray to white contours indicate 1, 2 and 3- σ intervals. The red points correspond to the best-fit values. The chains were shifted to the best-fit values of the parameters specified in Table 3, to allow for a better visual inspection of the uncertainties.

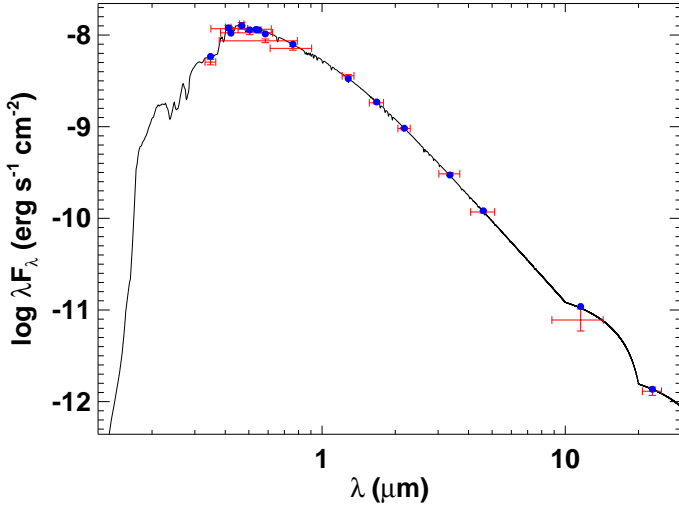


Fig. 7: Spectral energy distribution (SEDs) of WASP-33. Red symbols represent the observed photometric measurements, where the horizontal bars represent the effective width of the passband. Blue symbols are the model fluxes from the best-fit Kurucz atmosphere model (black).

tion that this joint model does not take into account a second order time-dependent polynomial to normalize the light curves. Its use did not only account for the lack of the phase curve model around primary transit, but also for imperfections in the photometry (namely residual pulsations and other systematics present in the SAP photometry, as previously discussed). In consequence, the planet-to-star radius ratio will appear slightly en-

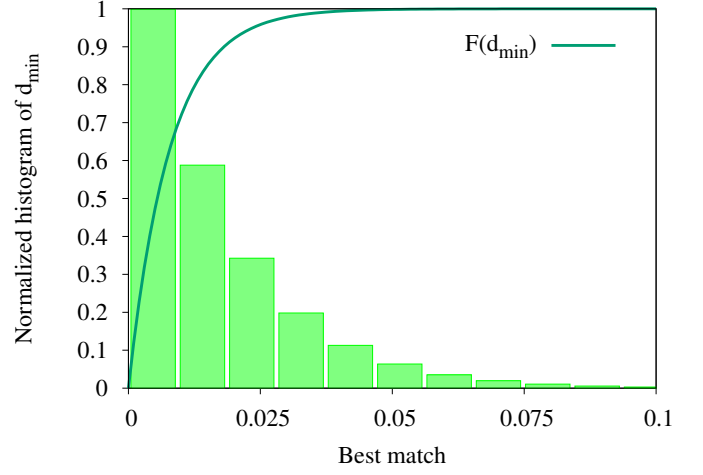


Fig. 8: Normalized histogram for the "best match" frequencies generated from 10^6 iterations, compared to $F(d_{\min})$, in continuous line.

larged to compensate for the lack of normalization. As starting values and standard deviation for the Gaussian priors we use the values listed in the third column of Table 3. To be conservative, the uncertainties were enlarged by a factor of 3.

4.3. Secondary eclipse model

As secondary eclipse model we consider a scaled version of the transit model given by Mandel & Agol (2002), with both linear and quadratic limb-darkening coefficients set to zero. The contribution of WASP-33's companion and the orbital eccentricity were considered in the same fashion as specified before. As described in von Essen et al. (2019b), the secondary eclipse model, SE(t), is given by:

$$SE(t) = [TM(t) - 1.] \times SF + 1, \quad (6)$$

where TM(t) corresponds to Mandel & Agol (2002)'s primary transit model, and SF corresponds to a scaling factor that scales the transit to meet the secondary eclipse depth. From this factor, the secondary eclipse depth is computed as $(R_P/R_S)^2 \times SF$, and its error is computed from error propagation between the two. The fitting parameters are those from the transit model and the scaling factor.

4.4. Phase curve model

As performed by, e.g., Cowan & Agol (2008) and Zhang et al. (2018) on WASP-33's Spitzer photometry, we modelled the reflection of starlight and thermal emission from the day side of the planet, here called planetary phase variability, PPV(t), as a series of first order expansions in sines and cosines:

$$PPV(t) = c_0 + c_1 \times \sin(2\pi t/P) + c_2 \times \cos(2\pi t/P). \quad (7)$$

The fitting parameters are the offset, c_0 , the amplitudes of the sine and cosine, c_1 and c_2 , respectively, and the orbital period, treated as equal. This linear combination of sines and cosines allow for a potential offset between the region of maximum brightness and the sub-stellar point.

4.5. Ellipsoidal variation

Gravitational effects of a close-in exoplanet over its host create a distortion of the star that results in photometric variations with minimum occurring twice per orbit, during primary transit and secondary eclipse. This effect is called ellipsoidal variation, and depends mainly on the properties of the stellar surface, the masses of planet and star, and their relative distances. The ellipsoidal variation of WASP-33 has an amplitude, A_{EV} , given by:

$$A_{EV} = \beta \frac{M_P}{M_S} \left(\frac{R_S}{a} \right)^3, \quad (8)$$

(Loeb & Gaudi 2003). Here, M_P and M_S correspond to the planetary and stellar masses, respectively, a/R_S is the semi-major axis scaled to the stellar radius, and β (Morris 1985) depends on the limb-and-gravity darkening coefficients. For WASP-33A and b, $A_{EV} = 27.4$ ppm. The limb-and-gravity darkening coefficients were taken from Claret (2017), interpolated to the stellar parameters of WASP-33, and the mass of WASP-33b was taken from Lehmann et al. (2015) with $M_P = 2.1 \pm 0.2 M_J$. The remaining parameters were taken from this work. For this model component the fitting parameters are those connected to $TM(t)$, treated as equal, and the planetary mass.

4.6. Doppler beaming

Both planet and star orbit around their common barycenter. While doing so, the star will periodically move towards and away from the observer. This creates a variation of the brightness of the host star in total sync with the frequency of the planet. The amplitude of the Doppler beaming is given by:

$$A_{DB} = (3 - \alpha) \frac{K_{RV}}{c}, \quad (9)$$

(Rybicki & Lightman 1979), where α is defined in Loeb & Gaudi (2003), K_{RV} is the radial velocity amplitude of the planet, and c is the speed of light. For WASP-33, $A_{DB} = 2.7$ ppm. As in the case of the ellipsoidal variation, the fitting parameters are those connected to $TM(t)$ and the planetary mass, which is treated as equal to the mass from the ellipsoidal variation.

Figure 9 shows the thermal emission and reflected light, the ellipsoidal variation (EV) and the Doppler beaming (DB) for WASP-33b, to allow for a comparison of the amplitudes of the different effects. Even though the phase curve model is shown along the whole orbital phase, in our joint fit it is turned off during secondary eclipse, as the planet is blocked by the star and, in consequence, does not produce any signal. As previously mentioned, in Table 5 we provide four sets of results, with uniform and Gaussian priors, and with and without fitting for the planetary mass.

4.7. Impact of the pulsations over the derived secondary eclipse depth and phase curve amplitude

As reported in Sect. 3.3, 29 pulsations showed a significant signal above the noise and were, in consequence, detected as such. From Period04 we extracted the corresponding frequencies, amplitudes and phases, that were used to clean the data from pulsations to recover the planetary signature. To do so, similarly to von Essen et al. (2014, 2015) we considered as pulsation model Eq. 4. The pulsation amplitudes listed in the top of the table are comparable –or even larger– to the expected eclipse depth. Instead of considering them as noise, we carried out a thorough

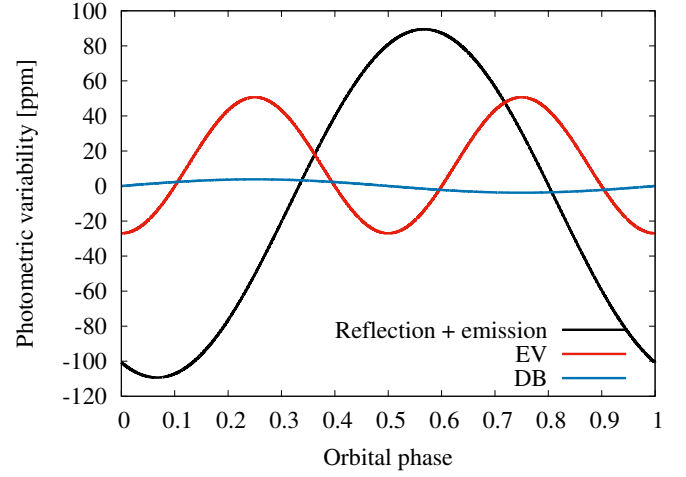


Fig. 9: Photometric variability in ppm given by reflection and emission in black continuous line, ellipsoidal variation (EV) in red dotted line and Doppler beaming (DB) in blue dashed line, as derived in this work. Values are placed around zero to allow for visual comparison.

analysis of their impact over the planetary signature. As a counterpart, several high frequency pulsations reported in this work have amplitudes smaller than 100 ppm, lying at the limit or even below TESS point-to-point scatter. In consequence, these pulsations might be statistically irrelevant when including them as part of our model budget, which was analyzed, too.

Using Period04, we computed pulsation-corrected light curves (PCLCs) taking into account sub-groups of pulsations, namely the full set, and those with the 25, 20, 15, 10, 9, 8, 7, 6, 5, 4, 3, 2 and 1 highest amplitudes. The difference in step serves as a way to carry out a more detailed investigation of the impact the pulsation frequencies with the highest amplitudes have. We ended up with 14 PCLCs, each one of them with a different “pulsation noise” level. We prefer to use Period04 residuals because MCMC fits are time-consuming. The former has been shown to deliver robust results as far as pulsation frequency analysis concerns.

To test if the chosen number of pulsations has an impact in the determination of the physical properties of WASP-33b, for each one of the 14 PCLCs we repeated the same process. To speed up the process, we subtracted the primary transit model evaluated in the parameters reported in Table 3, plus the ellipsoidal variation and the Doppler beaming that were evaluated considering the mass value given by Lehmann et al. (2015). Thus, we carried out an MCMC fit between the PCLCs and the phase curve and secondary eclipse models specified before. In each case we computed the best-fit parameters and their uncertainties, along with the standard deviation of the residuals (PCLCs minus best-fit $SE(t) + PPV(t)$ model) and the Bayesian Information Criterion, $BIC = \chi^2 + k \ln(N)$. For the BIC, χ^2 is computed in the usual way, between the PCLCs and the best-fit model. N corresponds to the total length of the photometry, and k is the number of fitting parameters. For k we considered the usual four parameters (SF , c_0 , c_1 and c_2), plus $3 \times PN$, being PN the number of pulsations considered in each sub-group of PCLCs. The factor 3 accounts for each frequency, amplitude and phase.

Fig. 10 shows the evolution of the BIC, the standard deviation of the residuals, and some of the fitted parameters, specifi-

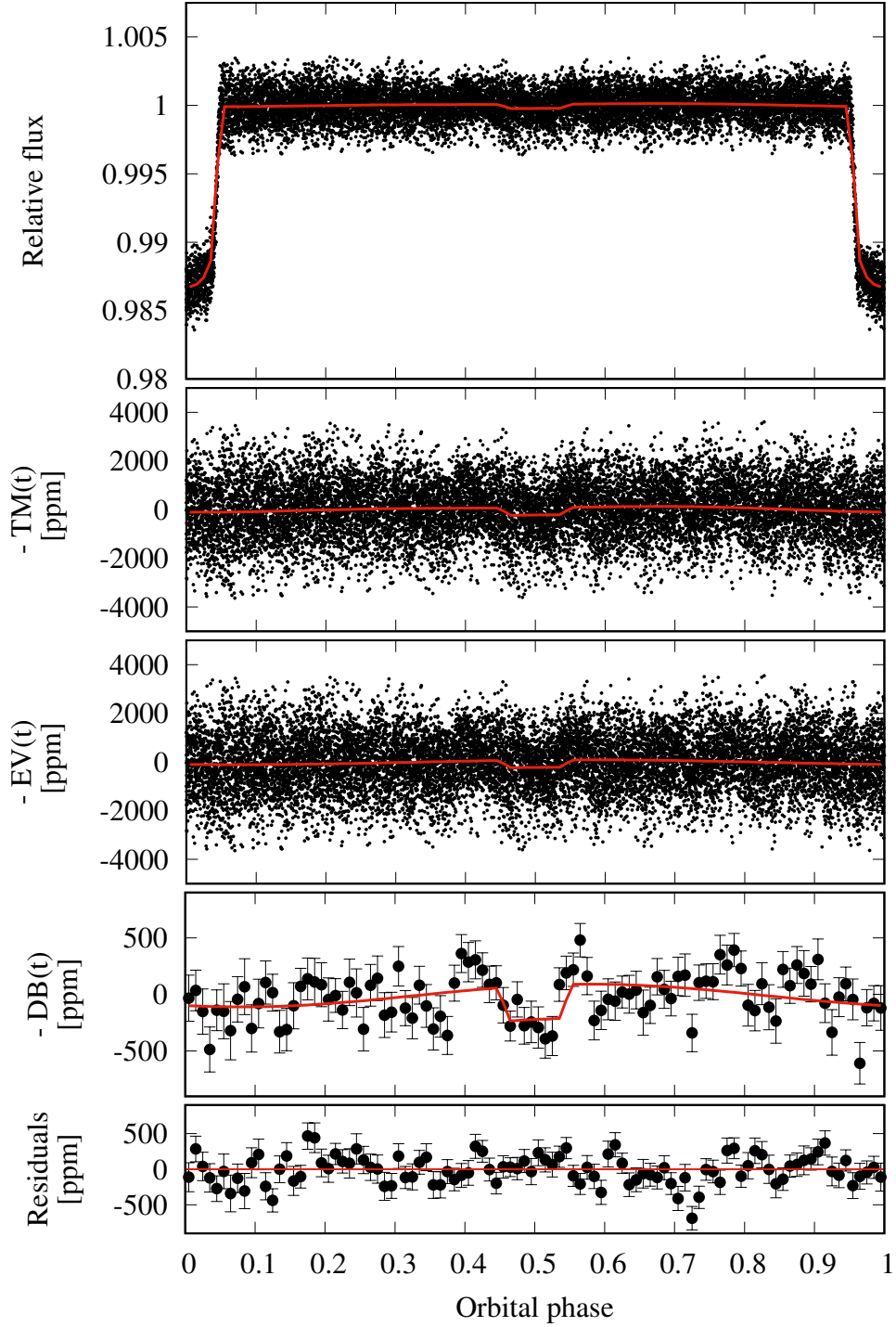


Fig. 11: From top to bottom: phase-folded light curve of WASP-33 in black points showing the primary transit around phases 0,1 and the residual pulsations of the host star; relative flux of WASP-33 in parts per million (ppm) once the primary transit model (TM, second panel), the ellipsoidal variation (EV, third panel), and the Doppler beaming (DB, fourth panel) were removed. The last two panels show the data binned at $\phi = 0.01$ with the secondary eclipse plus phase curve on top, and the residuals from the best-fit model on the bottom. Red lines always show the different components of the best-fit model.

Table 4: Best-fit values and $1-\sigma$ uncertainties for the parameters accompanying among others the Mandel & Agol (2002) model, a/R_S , i , R_P/R_S , P , and T_0 , the phase curve, c_0 , c_1 and c_2 , and the scaling factor of the secondary eclipse model, SF. In addition, the amplitude of the phase curve, A , the eclipse depth, ED, and the offset between the region of maximum brightness and the sub-stellar point, ϕ_{off} . Values are given, from left to right, for M1, M2, M3 and M4.

Parameter	M1	M2	M3	M4
a/R_S	3.601 ± 0.005	3.600 ± 0.005	3.603 ± 0.005	3.600 ± 0.005
i ($^\circ$)	88.53 ± 0.21	88.53 ± 0.22	88.52 ± 0.22	88.52 ± 0.23
R_P/R_S	0.1087 ± 0.0002	0.1087 ± 0.0002	0.1086 ± 0.0002	0.1087 ± 0.0002
P (days)	$1.2198705 \pm 3.7 \times 10^{-6}$	$1.2198706 \pm 3.7 \times 10^{-6}$	$1.2198706 \pm 3.9 \times 10^{-6}$	$1.2198704 \pm 3.8 \times 10^{-6}$
T_0 (BJD _{TDB})	$2458792.63405 \pm 0.00006$	$2458792.63405 \pm 0.00006$	$2458792.63405 \pm 0.00005$	$2458792.63405 \pm 0.00005$
c_0 (ppm)	1 ± 10	3 ± 10	-56 ± 19	-9 ± 12
c_1 (ppm)	45.4 ± 12.2	47.4 ± 10.7	52.8 ± 12.2	48.3 ± 12.1
c_2 (ppm)	87.7 ± 15.1	90.5 ± 14.9	87.4 ± 13.1	88.1 ± 13.4
SF	0.0189 ± 0.0027	0.0270 ± 0.0031	0.0220 ± 0.0035	0.0258 ± 0.0030
ED (ppm)	223.9 ± 31.0	320.4 ± 37.2	259.4 ± 41.0	305.8 ± 35.5
A (ppm)	98.7 ± 14.7	102.1 ± 14.1	102.1 ± 12.8	100.4 ± 13.1
ϕ_{off} ($^\circ$)	27.3 ± 7.6	27.7 ± 6.6	31.1 ± 7.0	28.7 ± 7.1
M_P (M_J)	-	-	5.7 ± 1.2	2.81 ± 0.53
χ	17273	16101	17269	16100
BIC	17359	16187	17364	16192
χ^2_{red}	1.2316	1.1541	1.2314	1.1541
Degrees of freedom	9	9	10	10

mass is not a fitting parameter. However, the $\Delta\text{BIC} = -5$ compared to model M4 does not favor M2 significantly. To emphasize the additional benefit of an independent mass measurement for WASP-33b from the phase curve photometry, we will discuss the results of M4 in the remainder of this paper. Nonetheless, it is worth to mention that the use of uniform and Gaussian priors on the mass of the planet returned different results. We believe it is because TESS data, even though extremely rich, do not allow for a completely independent determination of the planetary mass, without previous knowledge of it. Posterior probability distributions for the fitted parameters can be seen in Fig. B.1 for M4 only, as all posteriors look alike.

5.2. Physical parameters derived from these observations

Following the prescription given by Cowan & Agol (2011), from our derived parameters we computed the Bond albedo,

$$A_B = 1 - \frac{5T_n^4 + 3T_d^4}{2T_o^4}, \quad (12)$$

and the heat redistribution efficiency,

$$\epsilon = \frac{8}{5 + 3(T_d/T_n)^4} \quad (13)$$

where T_d and T_n correspond to the temperature of the day side and the night side, respectively. To compute the day side temperature we made use of the secondary eclipse depth divided by the primary transit depth, as this is a direct measure of the ratio of the planetary day side intensity to the stellar intensity, $\psi(\lambda)_{\text{day}} = \text{ED}/(R_P/R_S)^2 = \text{SF}$. Equivalently to this, to compute the night side temperature we used the difference between the secondary eclipse depth and the phase variation amplitude, combined with the offset between the region of maximum brightness and the substellar point, $\psi(\lambda)_{\text{night}} = \text{ED} - 2A \times \cos(\phi_{\text{off}})$. We then computed the brightness temperature of the planet following the prescription given in Cowan & Agol (2011),

$$T_b(\lambda) = \frac{hc}{\lambda k} \left[\log \left(1 + \frac{e^{hc/\lambda k T_{*b}(\lambda)} - 1}{\psi(\lambda)} \right) \right]^{-1}. \quad (14)$$

Here, $T_{*b}(\lambda)$ is the star's brightness temperature within TESS passband, equal to 7337 K, and h , c and k are the Planck constant, the speed of light, and the Boltzmann constant, respectively. Table 5 summarizes the values derived in this work, compared to the ones computed by Zhang et al. (2018). Results for all modelling approaches are provided, to show robustness in our analysis.

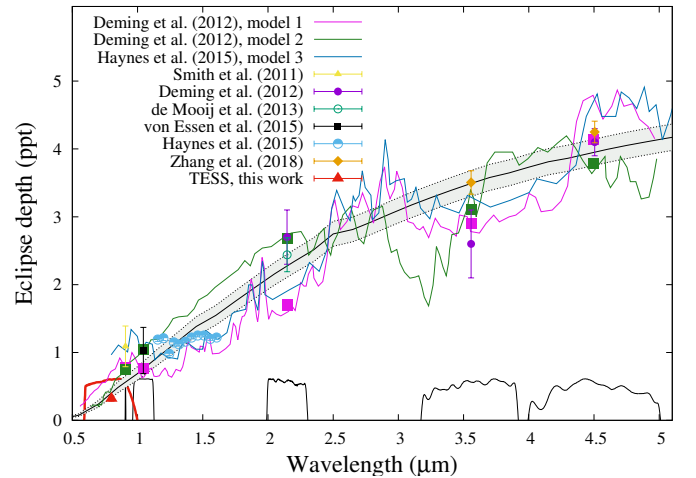


Fig. 12: Eclipse depth, in ppt, as a function of wavelength. The red triangle corresponds to TESS value, reported in this work. The gray area shows $1-\sigma$ contour of the equilibrium temperature of WASP-33b. Literature measurements come from Smith et al. (2011) (yellow triangle) Deming et al. (2012) (violet circles), de Mooij et al. (2013) (empty green circle) von Essen et al. (2015) (black square), Haynes et al. (2015) (half-filled blue circles), Zhang et al. (2018) (yellow diamonds) and this work (red triangle). Transmission responses are plotted in black continuous lines, with the exception of TESS, highlighted in red.

We obtain uncertainties on these parameters using the posterior probability distributions for the values c_1 , c_2 and SF. In detail, for each one of the 8000 MCMC iterations we com-

Table 5: Bond albedo, recirculation efficiency and day and night side brightness temperatures for WASP-33b within the TESS passband derived from M1, M2, M3 and M4. Last column shows the averaged values reported by Zhang et al. (2018) from Spitzer photometry.

Parameter	M1	M2	M3	M4	(Zhang et al. 2018)
T_{day} (K)	2881 ± 63	3037 ± 60	2934 ± 75	3014 ± 60	3144 ± 114
T_{night} (K)	1487 ± 95	1617 ± 39	1541 ± 73	1605 ± 45	1757 ± 88
A_B	0.473 ± 0.046	0.351 ± 0.049	0.434 ± 0.057	0.369 ± 0.050	$0.25^{+0.09}_{-0.10}$
ϵ	0.168 ± 0.030	0.189 ± 0.013	0.180 ± 0.021	0.189 ± 0.014	$0.22^{+0.03}_{-0.04}$

pute the Bond albedo, recirculation efficiency, and day and night side brightness temperature. In this way, the values reported in Table 5 are obtained from their median and standard deviation. Our values are fully consistent to the ones reported by Zhang et al. (2018). Fig. 12 shows our derived eclipse depth compared to literature measurements. Models 1 and 2 were taken from Deming et al. (2012) and correspond to a solar composition model with an inverted temperature in pink and a carbon-rich non-inverted model in green, respectively. Model 3 was taken from Haynes et al. (2015) and reflects their best-fit inversion model with TiO. To determine the effective temperature of WASP-33b we fitted all the literature values to synthetic eclipse depths. These were created integrating the flux ratio between a black body of different temperatures (the planet) and the PHOENIX intensities specified before (the star). From χ^2 minimization we obtained $T_{\text{eff},W33} = 3105 \pm 95$ K. The error on the temperature was computed considering $\Delta\chi^2 = 1$.

Fitting model M4, the TESS phase curve also allowed for an independent mass measurement of WASP-33b by a fit for the photometric variations due to gravitational interactions between planet and host star. We derive a value of $M_P = 2.85 \pm 0.51$ M_J, which is consistent with the value of Lehmann et al. (2015) estimated by radial velocity measurements within 1.5σ . A good agreement between photometric and radial velocity mass measurement was for example also achieved in the TESS full-orbit phase curve of WASP-18b (Shporer et al. 2019). However, there are examples in the literature of discrepant mass values of these independent methods, potentially related to an insufficient knowledge of the host star. We refer the reader to an extensive discussion on this issue in Shporer (2017).

5.3. WASP-33b in context

Theoretical calculations predicted an energy transport from the day side to the night side on hot Jupiters by winds (Showman & Guillot 2002; Perez-Becker & Showman 2013). Early Spitzer phase curve observations provided observational indications in line with these predictions by measuring an eastward offset between the hottest measured longitude and the most strongly irradiated longitude at the substellar point (e.g. Knutson et al. 2007, 2012). With increasing number of available Spitzer data, a trend was revealed of a less pronounced phase offset and an increasing temperature day-night contrast with increasing stellar insolation of the planet. It was understood as a reduced efficiency of the heat transport for hotter planets, caused by the balance between advective and radiative cooling, and drag forces decelerating the advection (e.g. Komacek et al. 2017). Surprisingly, two more recent observations of the ultra-hot Jupiters WASP-103b and WASP-33b showed comparably weakened temperature contrast between day and night sides (Kreidberg et al. 2018; Zhang et al. 2018). Bell & Cowan (2018) and Tan & Komacek (2019) explained this effect by taking into account the dissociation and recombination of hydrogen molecules, which plays a

role only for the very hottest known exoplanets. Our derived values for day and night brightness temperature, and subsequently ϵ , agree very well with the results of Zhang et al. (2018) for WASP-33b, thus they strengthen the indication of a turn around in day-night temperature contrast for the most insolated ultra-hot Jupiters. Also the TESS phase curve analysis of the hottest known gas giant, KELT-9b, by Wong et al. (2019) confirm such result. Associated to the same phenomenon, Keating et al. (2019) described an increase of the night side temperature with increasing stellar insolation, including the Zhang et al. (2018) temperature value of WASP-33b. Our result of this work is in line with this correlation.

The TESS light curve revealed a westward phase offset for WASP-33b, i.e. the maximum in brightness happened after the secondary eclipse. Such westward phase offsets have been spotted in hot Jupiter systems before. At NIR wavelengths, Spitzer 4.5 μm revealed an offset of 21 ± 4 degrees in CoRoT-2b, which was in turn not observed at 3.6 μm (Dang et al. 2018). To explain their observational evidences, the authors speculated three possible scenarios, divided among non-synchronous rotation, magnetic effects, or eastern clouds. Even more rare results were revealed by Kepler photometry in HAT-P-7b, because the observed phase offsets appeared to change in time (Armstrong et al. 2016). Assuming these changes were not caused by systematic noise over the data, Rogers (2017) explained them by magnetic interactions that could create phase offsets with periodic changes in position. For a hot Jupiter of more moderate temperature, Kepler-7b, the Kepler phase curves probe reflected light, hence the measured westward offset might be caused by a cloudy western hemisphere (Demory et al. 2013). Besides this work, another ultra-hot Jupiter showing a westward offset of ~ 14 degrees is WASP-12b (Bell et al. 2019). A recent collection of phase offset measurements are given in Keating et al. (2020), focused only on Spitzer data at 3.6 and 4.5 μm . Their figure 7 reveals a wide spread, with a clear preference for eastward offsets. However, about six targets present westward offsets, and of this sample, two present both eastward and westward phase offsets. For WASP-33b, the effective temperature is above 3000 K. In consequence, TESS wavelengths must be probing mostly thermal emission and to a least extent, reflected light. In consequence, the observed westward offset could be explained by the same three hypotheses presented by Dang et al. (2018) on CoRoT-2b. However, in order to consolidate the observed eastward offset by Zhang et al. (2018) in Spitzer 4.5 and 3.6 μm with our detected westward offset in TESS light, time-variable clouds or magnetic fields would be the best explanations. All these mixed-up results might be pointing at the fact that the atmospheric dynamics of hot and ultra-hot Jupiters are more complicated than we thought.

We add an additional word of caution. In an earlier stage of our data analysis of this work, we carried out fits of the different model components in independent steps, rather than in simultaneous as presented here. The resulting phase offset we obtained

was actually eastwards and consistent with the one detected by Zhang et al. (2018). In consequence, we might consider that phase offsets are prone to details in the analysis or systematics in the data. The robust extraction of the phase offset from photometric data might be more challenging than what we thought. As WASP-33's photometry is affected by intrinsic variability of the host star, we can not reject a non-astrophysical origin of the westward phase offset.

The consistency in the measured day side temperature between the optical phase curve analyzed in this work and the near-IR phase curves of Zhang et al. (2018) indicate a thermal emission of the WASP-33b day side being similar to a black body, potentially caused by the continuum opacity of the hydrogen anion H^- (Arcangeli et al. 2018; Kitzmann et al. 2018). However, the phase offset measured in this work of $\phi_{\text{off}} = 24 \pm 8$ degrees deviates significantly from the negative (eastward) offset measured by Zhang et al. (2018) in the near-infrared. If considered as a real astrophysical phenomenon in the planetary atmosphere, a future 3D general circulation modeling (e.g. Kreidberg et al. 2018; Arcangeli et al. 2019) might shed light on the underlying physical conditions.

Ultra-hot Jupiters like WASP-33b are expected to be cloud-free on their day sides since the atmospheres are too hot for condensates to form Wakeford et al. (2017). The lack of clouds should manifest by a low ability to reflect star light, thus a low value of geometric albedo. The amount of light reflected off the planet is included in the secondary eclipse depth, however it is merged with the light thermally emitted by the planet itself. To isolate and estimate the component of reflected light, we follow the approach of Mallonn et al. (2019) and approximate the thermal emission by a black body radiation of a temperature estimated from previous near-IR measurements. Pass et al. (2019) used Gaussian process regression to derive a black body temperature of 3108 K for WASP-33b based on the HST/WFC3 secondary eclipse depths of Haynes et al. (2015) and the Spitzer results of Zhang et al. (2018). The stellar effective temperature is 7430 K (Collier Cameron et al. 2010).

By Equation 3 of Mallonn et al. (2019), we estimate a geometric albedo of -0.04 ± 0.04 , thus the 3σ upper limit corresponds to 0.08. This low value of the geometric albedo is in line with the theoretical expectation of no reflection because the temperature on the day side is too hot to form condensates. It also agrees with the generally rather low measured optical values of other hot Jupiters by the Kepler satellite (e.g. Esteves et al. 2015; Angerhausen et al. 2015), and the ground-based z' band upper limits derived by Mallonn et al. (2019). However, the low geometric albedo contrasts to the substantial value of Bond albedo given in Table 5. Future secondary eclipse measurements near the wavelength of stellar peak emission at 400 nm might shed light on this issue. The null-detection of the geometric albedo proves that the TESS phase curve of WASP-33b is dominated by thermal emission compared to reflected light. The opposite was recently found in the TESS phase curve of WASP-19b (Wong et al. 2020), showing a significantly non-zero albedo and dominating reflected light.

The approximation of the planetary thermal emission by a black body is valid for the derivation of an upper limit of the geometric albedo, since more sophisticated emission modeling mostly points towards even higher thermal flux in the optical for ultra-hot Jupiters (Haynes et al. 2015; Mikal-Evans et al. 2019; Bourrier et al. 2019; Daylan et al. 2019). Higher thermal flux would translate into lower reflected light for a given value of the eclipse depth, therefore an upper limit of the reflected light component remains unaffected (Mallonn et al. 2019). We note

that in the case of TiO absorption at optical wavelengths, suggested by Haynes et al. (2015) and Nugroho et al. (2017), the optical eclipse depth is predicted to be deeper than measured in this work with a value of ~ 1000 ppm in the red part of the TESS bandpass (see Figure 5 in Haynes et al. 2015). Hence, the TESS secondary eclipse depth seems to disfavor the best fit model of Haynes et al. (2015) including TiO and a temperature inversion. However, since this indication is based on multiple individual publications of secondary eclipse depth in different wavelength regions, we suggest a homogeneous re-analysis of these data sets before drawing a clear conclusion, which is out of scope of this work. Our suggestion is strengthened by our result of Section 4.7 that the eclipse depth is affected by the number of pulsations included in the modeling. All previous work on secondary eclipses treat the pulsations in a different way, thus a homogeneous re-analysis appears useful.

6. Conclusion

In this work we present the first optical phase curve and secondary eclipse observations of WASP-33b, obtained from analyzing 23 days of TESS photometry. From both the secondary eclipse depth, $ED = 305.8 \pm 35.5$ ppm, the amplitude of the phase curve, $A = 100.4 \pm 13.1$ ppm, and the offset between the region of maximum brightness and the substellar point of 28.7 ± 7.1 degrees, we use a simple model to derive the brightness temperatures, $T_{\text{day}} = 3014 \pm 60$ K and $T_{\text{night}} = 1605 \pm 45$ K, Bond albedo $A_B = 0.369 \pm 0.050$ and recirculation efficiency, $\epsilon = 0.189 \pm 0.014$. While the low geometric albedo of below 0.08 (3σ upper limit) is consistent with other hot Jupiters, the rather high recirculation efficiency is consistent with previous WASP-33b studies at NIR wavelengths and points towards the possibility of the dissociation and recombination of hydrogen molecules in the atmospheres of ultra-hot Jupiters. Additionally, the high photometric precision in the phase-folded TESS data allowed for a mass measurement by the photometric variations caused by gravitational interactions. This mass is in good agreement with the literature value obtained from radial velocity measurements. Due to the nature of TESS continuous monitoring over WASP-33, we characterize the pulsation spectrum of the host star, finding 29 peaks with amplitude signal-to-noise ratio higher or equal to 4, instead of the 8 known so far. The newly unveiled low-frequency range of the star revealed two frequencies lower than 3 cd^{-1} that are consistent with gravity modes as observed in γ Doradus stars, making WASP-33 a γ Doradus/ δ Scuti hybrid candidate. However, more data is required to confirm this candidacy. Paying special attention in the way the pulsation frequencies are considered while determining planetary parameters, we find that using solely the minimization of the BIC to quantify the amount of pulsation frequencies to be considered in our model does not provide correct planetary parameters. Special care has to be taken into the pulsations with the highest amplitude. Future detailed asteroseismic analyses of WASP-33 could help to improve the stellar parameters and better understand possible star-planet interactions (or the lack thereof).

Acknowledgements

We thank the referee for an outstanding quick reply, given the times, and for contributing to significantly improve our work. CvE and GT acknowledge support from the European Social Fund (project No. 09.3.3-LMT-K-712-01-0103) under grant agreement with the Lithuanian Science Council (LMTLT).

Funding for the Stellar Astrophysics Centre is provided by The Danish National Research Foundation (Grant agreement no.: DNRF106). This work was supported by a research grant (00028173) from VILLUM FONDEN.

References

- Adams, E. R., Dupree, A. K., Kulesa, C., & McCarthy, D. 2013, *AJ*, 146, 9
- Aerts, C., Christensen-Dalsgaard, J., & Kurtz, D. W. 2010, *Asteroseismology*
- Angelov, T. 1996, *Bulletin Astronomique de Belgique*, 154, 13
- Angerhausen, D., DeLarme, E., & Morse, J. A. 2015, *PASP*, 127, 1113
- Antoci, V., Cunha, M. S., Bowman, D. M., et al. 2019, *MNRAS*, 490, 4040
- Arcangeli, J., Désert, J.-M., Line, M. R., et al. 2018, *ApJ*, 855, L30
- Arcangeli, J., Désert, J.-M., Parmentier, V., et al. 2019, *A&A*, 625, A136
- Armstrong, D. J., de Mooij, E., Barstow, J., et al. 2016, *Nature Astronomy*, 1, 0004
- Balona, L. A. & Dziembowski, W. A. 2011, *MNRAS*, 417, 591
- Beatty, T. G., Marley, M. S., Gaudi, B. S., et al. 2019, *AJ*, 158, 166
- Bell, T. J. & Cowan, N. B. 2018, *ApJ*, 857, L20
- Bell, T. J., Zhang, M., Cubillos, P. E., et al. 2019, *MNRAS*, 489, 1995
- Belokurov, V., Penoyre, Z., Oh, S., et al. 2020, *arXiv e-prints*, arXiv:2003.05467
- Bouma, L. G., Winn, J. N., Baxter, C., et al. 2019, *AJ*, 157, 217
- Bourrier, V., Kitzmann, D., Kuntzer, T., et al. 2019, *arXiv e-prints*, arXiv:1909.03010
- Bowman, D. M. & Kurtz, D. W. 2018, *MNRAS*, 476, 3169
- Breger, M., Handler, G., Garrido, R., et al. 1999, *A&A*, 349, 225
- Breger, M., Stich, J., Garrido, R., et al. 1993, *A&A*, 271, 482
- Carter, J. A. & Winn, J. N. 2009, *ApJ*, 704, 51
- Claret, A. 2017, *A&A*, 600, A30
- Claret, A. & Bloemen, S. 2011, *A&A*, 529, A75
- Collier Cameron, A., Guenther, E., Smalley, B., et al. 2010, *MNRAS*, 407, 507
- Cowan, N. B. & Agol, E. 2008, *ApJ*, 678, L129
- Cowan, N. B. & Agol, E. 2011, *ApJ*, 729, 54
- Dang, L., Cowan, N. B., Schwartz, J. C., et al. 2018, *Nature Astronomy*, 2, 220
- Daylan, T., Günther, M. N., Mikal-Evans, T., et al. 2019, *arXiv e-prints*, arXiv:1909.03000
- de Mooij, E. J. W., Brogi, M., de Kok, R. J., et al. 2013, *A&A*, 550, A54
- Deming, D., Fraine, J. D., Sada, P. V., et al. 2012, *ApJ*, 754, 106
- Demory, B.-O., de Wit, J., Lewis, N., et al. 2013, *ApJ*, 776, L25
- Dragomir, D., Teske, J., Günther, M. N., et al. 2019, *ApJ*, 875, L7
- Esteves, L. J., De Mooij, E. J. W., & Jayawardhana, R. 2015, *ApJ*, 804, 150
- Gaia Collaboration, Brown, A. G. A., Vallenari, A., et al. 2018, *A&A*, 616, A1
- Grigahcène, A., Antoci, V., Balona, L., et al. 2010, *ApJ*, 713, L192
- Günther, M. N., Pozuelos, F. J., Dittmann, J. A., et al. 2019, *Nature Astronomy*, 3, 1099
- Gttingen, G.-A.-U. 2018, *Gttingen Spectral Library by PHOENIX*
- Hambleton, K. M., Kurtz, D. W., Prša, A., et al. 2013, *MNRAS*, 434, 925
- Haynes, K., Mandell, A. M., Madhusudhan, N., Deming, D., & Knutson, H. 2015, *ApJ*, 806, 146
- Herrero, E., Morales, J. C., Ribas, I., & Naves, R. 2011, *A&A*, 526, L10
- Jansen, T. & Kipping, D. 2020, *arXiv e-prints*, arXiv:2001.10580
- Jenkins, J. M. 2017, *Kepler Data Processing Handbook: KSCI-19081-002*, Tech. rep.
- Jenkins, J. M., Twicken, J. D., McCaulliff, S., et al. 2016, *Society of Photo-Optical Instrumentation Engineers (SPIE) Conference Series*, Vol. 9913, The TESS science processing operations center, 99133E
- Jones, E., Oliphant, T., Peterson, P., et al. 2001, *SciPy: Open source scientific tools for Python*, <http://www.scipy.org>
- Kass, R. E. & Raftery, A. E. 1995, *Journal of the American Statistical Association*, 90, 773
- Keating, D., Cowan, N. B., & Dang, L. 2019, *Nature Astronomy*, 3, 1092
- Keating, D., Stevenson, K. B., Cowan, N. B., et al. 2020, *arXiv e-prints*, arXiv:2004.00014
- Kitzmann, D., Heng, K., Rimmer, P. B., et al. 2018, *ApJ*, 863, 183
- Knutson, H. A., Charbonneau, D., Allen, L. E., et al. 2007, *Nature*, 447, 183
- Knutson, H. A., Lewis, N., Fortney, J. J., et al. 2012, *ApJ*, 754, 22
- Komacek, T. D., Showman, A. P., & Tan, X. 2017, *ApJ*, 835, 198
- Kostov, V. B., Schlieder, J. E., Barclay, T., et al. 2019, *AJ*, 158, 32
- Kreidberg, L., Line, M. R., Parmentier, V., et al. 2018, *AJ*, 156, 17
- Lehmann, H., Guenther, E., Sebastian, D., et al. 2015, *A&A*, 578, L4
- Lenz, P. & Breger, M. 2005, *Communications in Asteroseismology*, 146, 53
- Li, G., Van Reeth, T., Bedding, T. R., et al. 2020, *MNRAS*, 491, 3586
- Loeb, A. & Gaudi, B. S. 2003, *ApJ*, 588, L117
- Lothringer, J. D., Barman, T., & Koskinen, T. 2018, *ApJ*, 866, 27
- Maciejewski, G., Fernández, M., Aceituno, F., et al. 2018, *Acta Astron.*, 68, 371
- Mallonn, M., Köhler, J., Alexoudi, X., et al. 2019, *A&A*, 624, A62
- Mandel, K. & Agol, E. 2002, *ApJ*, 580, L171
- Mikal-Evans, T., Sing, D. K., Goyal, J. M., et al. 2019, *MNRAS*, 488, 2222
- Morris, S. L. 1985, *ApJ*, 295, 143
- Moya, A., Bouy, H., Marchis, F., Vicente, B., & Barrado, D. 2011, *A&A*, 535, A110
- Mugrauer, M. 2019, *MNRAS*, 490, 5088
- Ngo, H., Knutson, H. A., Hinkley, S., et al. 2016, *ApJ*, 827, 8
- Nugroho, S. K., Kawahara, H., Masuda, K., et al. 2017, *AJ*, 154, 221
- Parmentier, V. & Crossfield, I. J. M. 2018, *Exoplanet Phase Curves: Observations and Theory*, 116
- Pass, E. K., Cowan, N. B., Cubillos, P. E., & Sklar, J. G. 2019, *MNRAS*, 489, 941
- Patil, A., Huard, D., & Fonnesbeck, C. J. 2010, *Journal of Statistical Software*, 35, 1
- Paunzen, E. 2015, *A&A*, 580, A23
- Perez-Becker, D. & Showman, A. P. 2013, *ApJ*, 776, 134
- Piskorz, D., Knutson, H. A., Ngo, H., et al. 2015, *ApJ*, 814, 148
- Ricker, G. R., Winn, J. N., Vanderspek, R., et al. 2015, *Journal of Astronomical Telescopes, Instruments, and Systems*, 1, 014003
- Rodriguez, J. E., Quinn, S. N., Huang, C. X., et al. 2019, *AJ*, 157, 191
- Rogers, T. M. 2017, *Nature Astronomy*, 1, 0131
- Rybicki, G. B. & Lightman, A. P. 1979, *Astronomy Quarterly*, 3, 199
- Schlegel, D. J., Finkbeiner, D. P., & Davis, M. 1998, *ApJ*, 500, 525
- Showman, A. P. & Guillot, T. 2002, *A&A*, 385, 166
- Shporer, A. 2017, *PASP*, 129, 072001
- Shporer, A., Wong, I., Huang, C. X., et al. 2019, *AJ*, 157, 178
- Smith, A. M. S., Anderson, D. R., Skillen, I., Collier Cameron, A., & Smalley, B. 2011, *MNRAS*, 416, 2096
- Smith, J. C., Stumpe, M. C., Van Cleve, J. E., et al. 2012, *PASP*, 124, 1000
- Stassun, K. G., Collins, K. A., & Gaudi, B. S. 2017, *AJ*, 153, 136
- Stassun, K. G. & Torres, G. 2016, *AJ*, 152, 180
- Stassun, K. G. & Torres, G. 2018, *ApJ*, 862, 61
- Stumpe, M. C., Smith, J. C., Catanzarite, J. H., et al. 2014, *PASP*, 126, 100
- Tan, X. & Komacek, T. D. 2019, *ApJ*, 886, 26
- Torres, G., Andersen, J., & Giménez, A. 2010, *A&A Rev.*, 18, 67
- Uytterhoeven, K., Moya, A., Grigahcène, A., et al. 2011, *A&A*, 534, A125
- Vanderburg, A., Huang, C. X., Rodriguez, J. E., et al. 2019, *ApJ*, 881, L19
- von Essen, C., Cellone, S., Mallonn, M., et al. 2017, *A&A*, 603, A20
- von Essen, C., Czesla, S., Wolter, U., et al. 2014, *A&A*, 561, A48
- von Essen, C., Mallonn, M., Albrecht, S., et al. 2015, *A&A*, 584, A75
- von Essen, C., Mallonn, M., Welbanks, L., et al. 2019a, *A&A*, 622, A71
- von Essen, C., Stefansson, G., Mallonn, M., et al. 2019b, *A&A*, 628, A115
- Wakeford, H. R., Visscher, C., Lewis, N. K., et al. 2017, *MNRAS*, 464, 4247
- Welbanks, L., Madhusudhan, N., Allard, N. F., et al. 2019, *ApJ*, 887, L20
- Wöllert, M. & Brandner, W. 2015, *A&A*, 579, A129
- Wong, I., Benneke, B., Shporer, A., et al. 2020, *AJ*, 159, 104
- Wong, I., Shporer, A., Morris, B. M., et al. 2019, *arXiv e-prints*, arXiv:1910.01607
- Yan, F., Casasayas-Barris, N., Molaverdikhani, K., et al. 2019, *A&A*, 632, A69
- Zhang, M., Knutson, H. A., Kataria, T., et al. 2018, *AJ*, 155, 83

Appendix A: Primary transits photometry of WASP-33b

Appendix B: Posterior distributions

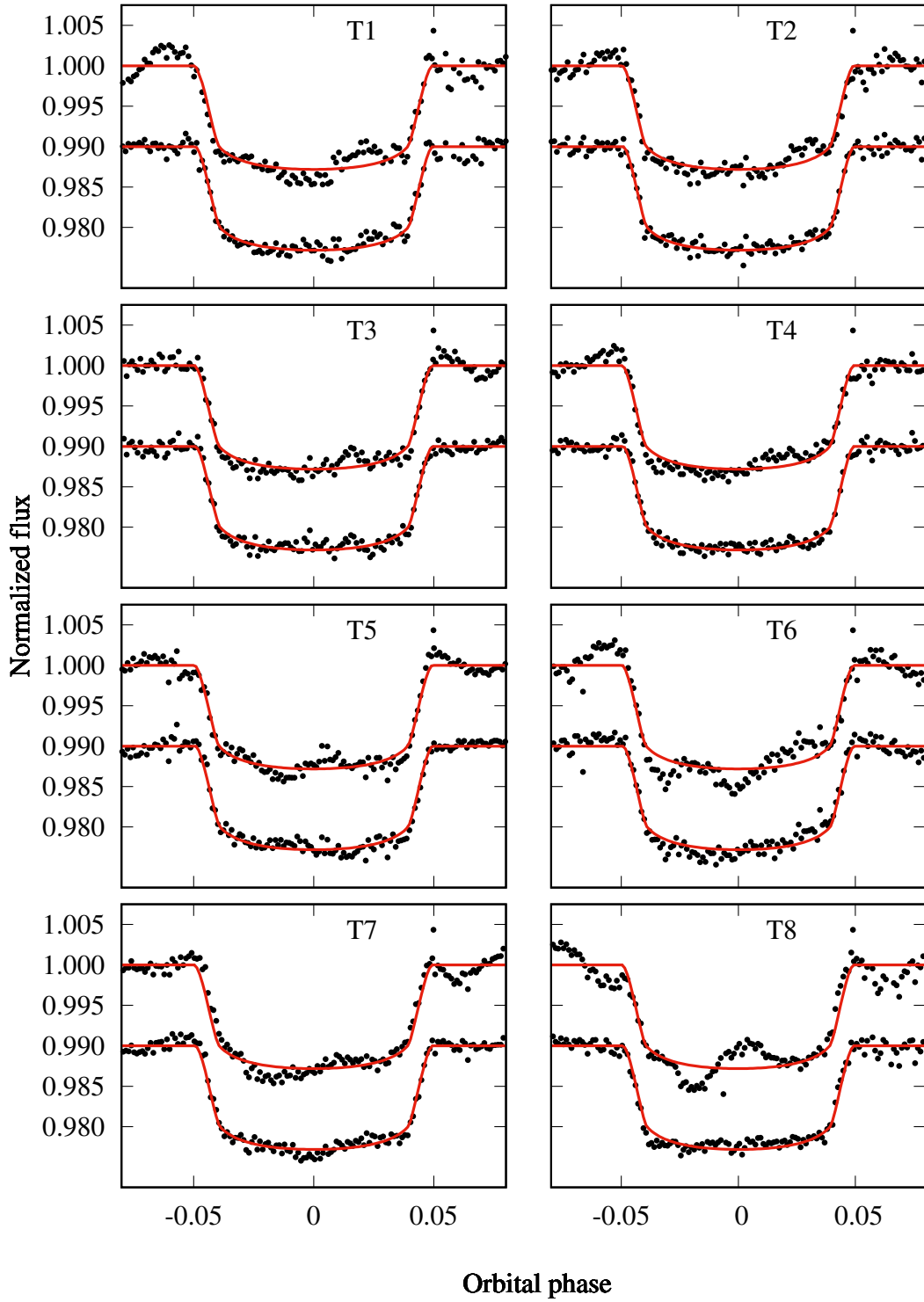


Fig. A.1: Normalized flux as a function of orbital phase for the primary transits of WASP-33b observed by TESS. From top to bottom and left to right time evolves. TESS observations are in black points, and the best-fit model in red continuous line. Individual error bars are not plotted to better visualize the effect of the pulsations over the photometry.

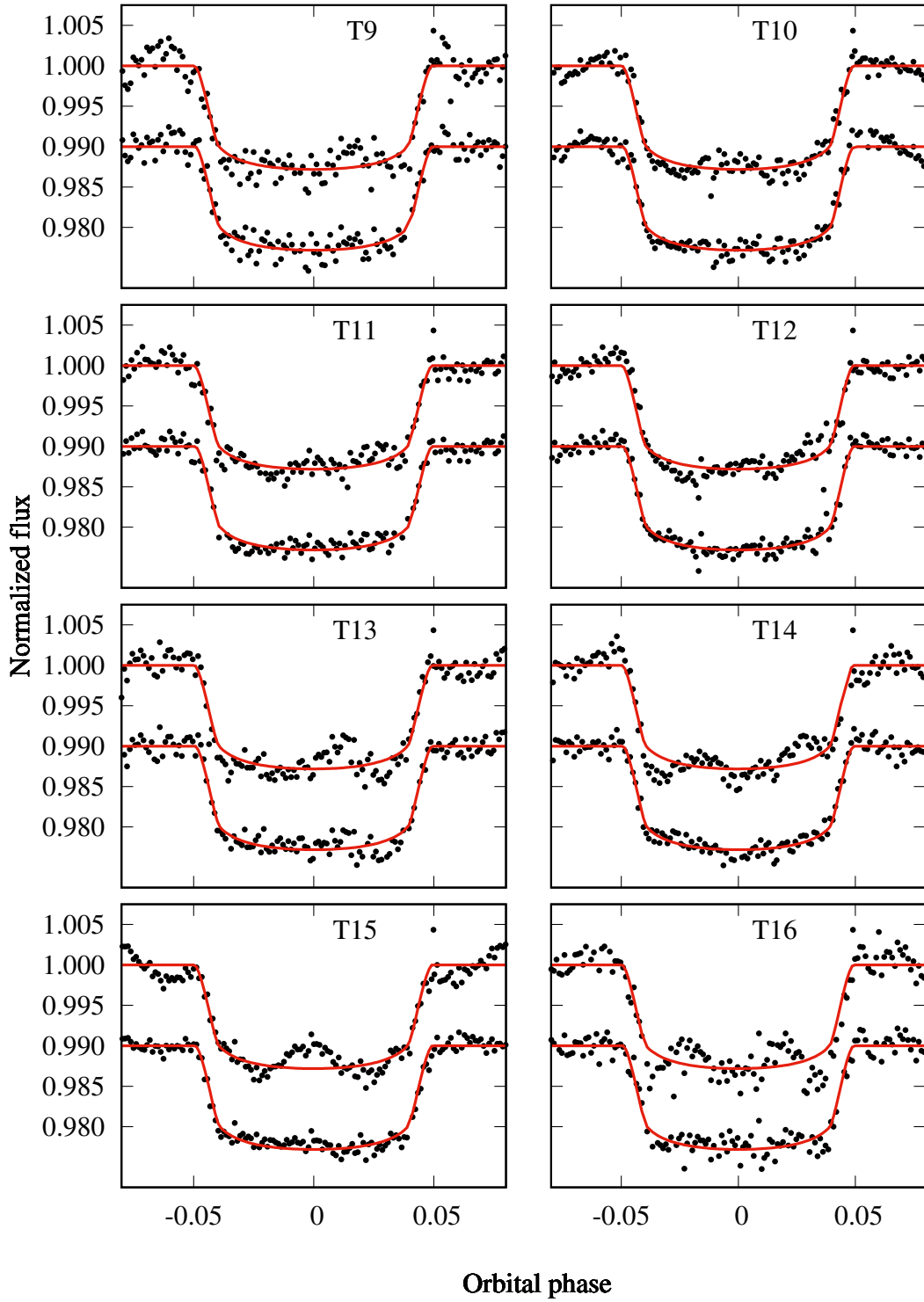


Fig. A.2: Same as Fig. A.1, but for the remaining 8 primary transits.

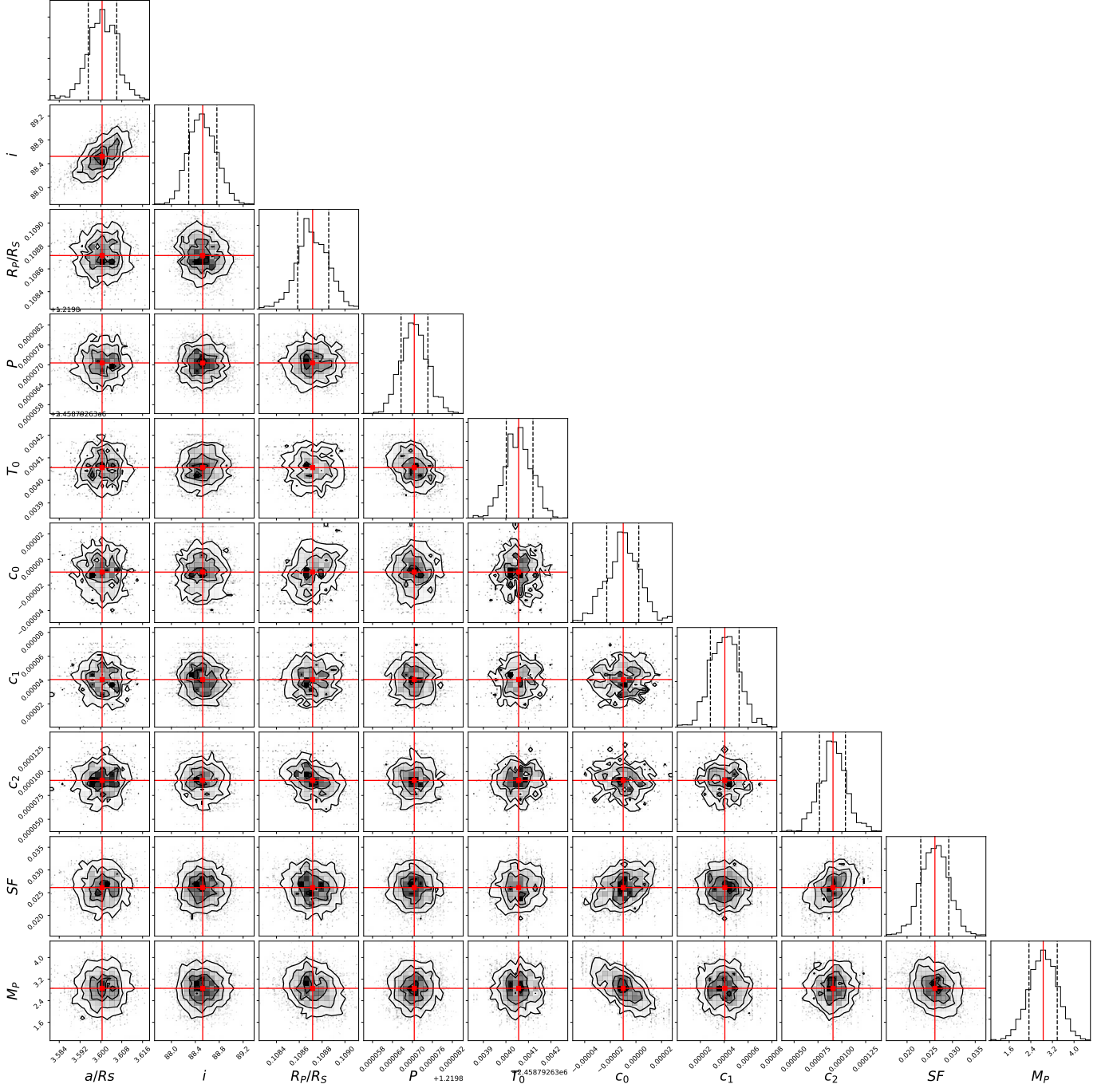


Fig. B.1: Posterior distributions for the fitted parameters specified in Table 4, specifically for M4.